



저작자표시-비영리-변경금지 2.0 대한민국

이용자는 아래의 조건을 따르는 경우에 한하여 자유롭게

- 이 저작물을 복제, 배포, 전송, 전시, 공연 및 방송할 수 있습니다.

다음과 같은 조건을 따라야 합니다:



저작자표시. 귀하는 원저작자를 표시하여야 합니다.



비영리. 귀하는 이 저작물을 영리 목적으로 이용할 수 없습니다.



변경금지. 귀하는 이 저작물을 개작, 변형 또는 가공할 수 없습니다.

- 귀하는, 이 저작물의 재이용이나 배포의 경우, 이 저작물에 적용된 이용허락조건을 명확하게 나타내어야 합니다.
- 저작권자로부터 별도의 허가를 받으면 이러한 조건들은 적용되지 않습니다.

저작권법에 따른 이용자의 권리는 위의 내용에 의하여 영향을 받지 않습니다.

이것은 [이용허락규약\(Legal Code\)](#)을 이해하기 쉽게 요약한 것입니다.

[Disclaimer](#)

이학박사학위논문

Theoretical study of spin-orbit coupling effects
in electronic structures:
Topological insulators and Rashba splittings

전자구조에서 스핀-궤도 결합 효과의
이론적 연구: 위상 절연체와 라쉬바 분리

2014년 8월

서울대학교 대학원

물리천문학부

김민성

Theoretical study of spin-orbit coupling effects
in electronic structures:

Topological insulators and Rashba splittings

전자구조에서 스핀-궤도 결합 효과의
이론적 연구: 위상 절연체와 라쉬바 분리

지도교수 임 지 순

이 논문을 이학박사 학위논문으로 제출함

2014년 5월

서울대학교 대학원

물리천문학부

김 민 성

김민성의 이학박사 학위논문을 인준함

2014년 6월

위원장 유 재 준 (인)

부위원장 임 지 순 (인)

위원 국 양 (인)

위원 이 규 철 (인)

위원 최 형 준 (인)

**Theoretical study of spin-orbit coupling effects
in electronic structures:
Topological insulators and Rashba splittings**

Minsung Kim

Supervised by

Professor **Jisoon Ihm**

A Dissertation

Submitted to the Faculty of

Seoul National University

in Partial Fulfillment of

the Requirements for the Degree of

Doctor of Philosophy

May 2014

Department of Physics and Astronomy

Graduate School

Seoul National University

Abstract

Spin-orbit coupling is the relativistic effect where the motion of an electron around an atomic nucleus produces the effective magnetic field that couples to the spin magnetic moment of the electron. In electronic band structures, there are two intriguing phenomena that originate from the spin-orbit coupling: topological insulator and Rashba splitting, which are the topics of this thesis.

Topological insulators are new quantum phases distinguished by the bulk band topology from normal insulators, which are characterized by the existence of robust topological boundary states. In the topological insulator part, we study the band topology of two-dimensional thin films. Firstly, we consider the topological quantum phase transitions by external electric fields in Sb_2Te_3 thin films. We find that the films are a topological insulator or a normal insulator depending on the film thicknesses and the band topology can be changed by applying external fields. Examples of the topological transition from a normal insulator to a topological insulator as well as that from a topological insulator to a normal insulator will be presented. Secondly, we investigate the possibility of inducing a topological insulator phase by introducing defect superstructures in SnTe thin films. It is found that if we choose the symmetry and density

of the defects appropriately, defect-induced narrow bands can have nontrivial band topology. Since the defect-induced bands have narrow band width, the band topology of the materials can be controlled by charge doping. The band topology is calculated by both directly calculating the \mathbb{Z}_2 invariant and checking the edge state configurations. The two theoretical propositions might be useful for the realization and control of the topological phases in practice.

The Rashba effect is the spin splitting in electronic band structures due to inversion symmetry breaking and spin-orbit coupling. In the Rashba splitting part, we consider the directional controllability of the Rashba splittings by ferroelectric switching. Specifically, we investigate the band structures of ferroelectric organic-inorganic hybrid metal halide perovskites. In these materials, the ferroelectric polarization is coupled to the Rashba band splitting. Thus the helical direction of the angular momentum texture in the Rashba bands can be reversed under the ferroelectric switching. Also, there appear two $S=1/2$ and $J=1/2$ bands simultaneously that have contrasting spin and orbital moments. This ferroelectric-coupled Rashba material will provide practically convenient mechanism for the manipulation of the spin degree of freedom by external fields.

Keywords: spin-orbit coupling, topological insulator, Rashba splitting, tight-binding approximation, density functional theory

Student Number: 2007-20407

Contents

Abstract	vii
1 Introduction	1
2 Basic theories and methods	4
2.1 Density Functional Theory	4
2.1.1 Kohn-Sham equation	4
2.1.2 Exchange-correlation functional	7
2.2 Spin-orbit coupling	10
2.2.1 Noncollinear spin	10
2.2.2 Relativistic equation and spin-orbit coupling	10
3 Topological insulators	15
3.1 Topological phase transitions in Sb_2Te_3 thin films by external electric fields	15
3.1.1 Introduction	15
3.1.2 Results and Discussion	17
3.1.3 Conclusions	27

3.1.4	Methods	27
3.2	Topological narrow bands in Sn-Te bilayers with defect super- structures	28
3.2.1	Introduction	28
3.2.2	Results and Discussion	30
3.2.3	Conclusions	46
3.2.4	Methods	46
4	Rashba splittings	48
4.1	Polarization-dependent angular momentum textures of $S = 1/2$ and $J = 1/2$ Rashba bands in ferroelectric hybrid metal halide perovskites	48
4.1.1	Introduction	48
4.1.2	Results and Discussion	52
4.1.3	Conclusions	68
4.1.4	Methods	71
5	Summary	72
	Bibliography	76
	Abstract in Korean	83

List of Figures

3.1	Atomic structure of Sb_2Te_3 3QLs with a schematic illustration of the external electric field.	18
3.2	Electronic band structures of Sb_2Te_3 thin films. (a) The band structure of Sb_2Te_3 3QLs near the Fermi energy. (b) Schematics for the band structure. The topological surface states (Dirac cones) of upper and lower surfaces (left) are present. The intersurface interaction opens a small energy gap (center). The external electric fields breaks the inversion symmetry (right).	19
3.3	Electronic band structures of Sb_2Te_3 3QLs with external fields. The band structures of Sb_2Te_3 3QLs near the Fermi energy are depicted with (a) $E_{\perp} = 0.03 \text{ V/\AA}$, (b) $E_{\perp} = 0.067 \text{ V/\AA}$ (c) $E_{\perp} = 0.15 \text{ V/\AA}$. The inset in (b) shows the band structure close to the Fermi energy.	23

3.4	The n-field configurations for Sb_2Te_3 3QLs with external fields. The n-field configurations are depicted with (a) $E_{\perp} = 0.03 \text{ V/\AA}$, (b) $E_{\perp} = 0.15 \text{ V/\AA}$. The empty circles represent +1 and the filled circles represent -1. The plaquettes with no circles represent 0. The sum of the n-field values in half the BZ (modulo 2) gives the \mathbb{Z}_2 invariant. Thus we have $\nu = 0$ in (a) and $\nu = 1$ in (b).	24
3.5	The EMLDOS for Sb_2Te_3 3QLs with external fields. The EMLDOS for the edge principal layer are presented with (a) $E_{\perp} = 0.0 \text{ V/\AA}$, (c) $E_{\perp} = 0.15 \text{ V/\AA}$. For comparison, the EMLDOS for the bulk principal layer are presented with (b) $E_{\perp} = 0.0 \text{ V/\AA}$, (d) $E_{\perp} = 0.15 \text{ V/\AA}$. In (c), the topological gapless edge states appear in the bulk energy gap.	26
3.6	Atomic structure of a Sn-Te bilayer. (a) Top view. (b) Side view. The Sn-Te bilayer forms a buckled honeycomb structure.	31
3.7	Electronic band structure of a Sn-Te bilayer.	32
3.8	Schematic illustration of topologically nontrivial narrow bands induced by the defect superstructure. (a) Defect-induced degenerate bands appear at the Fermi level (without SOC). (b) Topologically nontrivial narrow bands appear due to the spin-orbit splitting. (c) Electron doping case. (c) Hole doping case.	33
3.9	Atomic structure of the Sn-Te bilayer with the Sn vacancy superstructure.	35

3.10	Electronic structure of the Sn-Te bilayer with the Sn vacancy superstructure. (a) Band structure of the Sn-Te bilayer with Sn vacancies in 5×5 periodicity. (b) Band structure near the Fermi energy. (c) Band structure near the Fermi energy without SOC. The TNNBs have nontrivial \mathbb{Z}_2 invariants ($\nu = 1$).	36
3.11	The n-field configuration and wavefunction of the upper TNNBs. (a) The n-field configuration of the upper TNNBs showing the nontrivial band topology. (b) The absolute square of the wavefunction of the upper TNNBs at the Γ point.	37
3.12	EMLDOS for the Sn-Te bilayer with the Sn vacancy superstructure. (a) EMLDOS of the edge layer. (b) EMLDOS of the bulk layer. The topological gapless edge states appear in (a).	39
3.13	Band structure and EMLDOS for the Sn-Te bilayer with the Sn vacancy superstructure with two electrons doped. (a) The band structure, (b) EMLDOS of the edge layer, and (c) EMLDOS of the bulk layer are depicted for the two electron doping case.	40
3.14	Band structure and EMLDOS for the Sn-Te bilayer with the Sn vacancy superstructure with two holes doped. (a) The band structure, (b) EMLDOS of the edge layer, and (c) EMLDOS of the bulk layer are depicted for the two hole doping case.	41
3.15	Atomic structure of the Sn-Te bilayer with the Te vacancy, 3 Sb substitutions and a hole doping in 5×5 periodicity.	42

3.16	Electronic structure of the Sn-Te bilayer with the Te vacancy, the Sb substitution and a hole doping in 5×5 periodicity. (a) Band structure of the system. (b) Band structure near the Fermi energy.	43
3.17	EMLDOS for the Sn-Te bilayer with the Te vacancy, the Sb substitution and a hole doping in 5×5 periodicity. (a) EMLDOS of the edge layer. (b) EMLDOS of the bulk layer. The topological gapless edge states are present in (a).	44
3.18	Band structure and EMLDOS for the Sn-Te bilayer with the Te vacancy, the Sb substitution and an electron doping in 5×5 periodicity. (a) The band structure, (b) EMLDOS of the edge layer, and (c) EMLDOS of the bulk layer are depicted for the one electron doping case.	45
4.1	Schematic illustration of the switchable $S = 1/2$ and $J = 1/2$ Rashba effect via ferroelectric switching.	51
4.2	Tight-binding band structure. (a) TB band structure without the ISB field. (b) TB band structure with $\gamma_{spz}=-0.02$, $\gamma_{ppz}=-0.022$. The helical direction of the spin (orbital) angular momentum is denoted by CW or CCW in VBM (CBM) in (b). Here, CW and CCW mean clockwise and counter-clockwise, respectively.	61

4.3	Angular momentum texture from the tight-binding calculations.	
	(a) Angular momentum texture near the A point of BZ in CBM.	
	(b) Angular momentum texture near the A point of BZ in VBM.	
	The constant energy contours correspond to the energy cuts in Fig 4.2.	62
4.4	Atomic and electronic structure in the first-principles calculations. (a) Atomic structure of β -MAPbI ₃ . (b) Band structure of β -MAPbI ₃	65
4.5	Angular momentum texture from the first-principles calculations. (a) Angular momentum texture near the Γ point of BZ in CBM. (b) Angular momentum texture near the Γ point of BZ in VBM. The constant energy contours are calculated at VBM- ΔE and CBM+ ΔE , where $\Delta E \approx 0.05$ eV.	66
4.6	Band dispersion with different k_z . \vec{b}_3 denotes the reciprocal lattice vector along the z direction.	67
4.7	Relative helicity change between the two Rashba bands. (a) TB band structure with $\gamma_{spz}=-0.02$, $\gamma_{ppz}=0.04$. (b) TB band structure with $\gamma_{spz}=-0.02$, $\gamma_{ppz}=0.11$	69
4.8	Relative helicity change in the distorted CsPbI ₃ . (a) The band structure with $r = 0.0$. (b) The band structure with $r = 1.5$. (c) The band structure with $r = -1.5$	70

Chapter 1

Introduction

Spin-orbit coupling becomes important when we consider materials with heavy constituent atoms. The spin-orbit coupling can play a crucial role in electronic structures, resulting in qualitatively different physics. In this thesis, we will consider two interesting effects of spin-orbit coupling in electronic structures; one is a topological insulator and the other is the Rashba splitting.

Chapter 2 describes basic theories and methods. The principal theoretical approach is the first-principles calculation based on density functional theory. We discuss the formalism and theoretical details in this Chapter.

Chapter 3 deals with the topological insulators. Topological phases in physics have been known since the discovery of the quantum Hall effect. Recent studies have revealed that there are another topologically distinct phases in both two- and three-dimension with the time reversal symmetry, called topological insulators. Due to nontrivial bulk band topology, topological insulators have topologically protected robust boundary states. Topological insulators are new topological quantum phases, and the realization and manipulation of

the topological phases are important issues in both theoretical and practical aspects. In this chapter, we consider two topics: topological phase transitions under external electric fields and topological insulator phase with defect superstructures. In the first part, thin films of Sb_2Te_3 are considered and we investigate the topological phase transitions of the films under external fields. To exemplify the transitions from a normal insulator to a topological insulator and vice versa, we choose 3 and 4 quintuple layers of Sb_2Te_3 . In the second part, we examine the possibility of realizing a topological insulator phase by introducing periodic defects in a two-dimensional thin film. We consider a Sn-Te bilayer that has large enough strength of spin-orbit coupling, and show that it becomes a two-dimensional topological insulator when an appropriate defect superstructure is introduced. Also, we discuss topological phase transitions by charge doping in the system.

Chapter 4 concerns the Rashba splitting in ferroelectric hybrid metal halide perovskites. The Rashba splitting occurs when spin-orbit coupling is present under broken inversion symmetry. Typical examples are surfaces and interfaces with heavy atoms, but three-dimensional systems can be also considered if inversion symmetry breaking polarization exists. The hybrid halide perovskites are ferroelectric-coupled three-dimensional Rashba materials, where the helical angular momentum of the Rashba-split bands can be controlled by ferroelectric switching. This mechanism is a practically simple way to manipulate the Rashba bands. The halide perovskites have another interesting feature; they have two different Rashba band splittings at the same time. In view of the angular momentum texture, the valence band shows spin-dominant band

splitting whereas the conduction band shows orbital-dominant band splitting. We investigate the interplay of ferroelectricity and Rashba splitting in these material as well as the characteristic electronic structures of the valence and conduction band edge states.

Chapter 5 is the conclusion of this thesis. We give summary and perspectives of the studies on the topological insulators and Rashba materials.

Chapter 2

Basic theories and methods

2.1 Density Functional Theory

Density functional theory (DFT) is an *ab initio* theory to calculate electronic structures of atoms, molecules, and solids. The theory describes the electronic structures well when the correlation effect is not significant. In this section, we give an overview of the DFT formalism [3, 4].

2.1.1 Kohn-Sham equation

The theoretical (and mathematical) grounds for the density-based formulation is given by the Hohenberg-Kohn theorems [1], where the theorems guarantee the construction of the energy functional in terms of the density. But although the theorems ensure the existence of the functional, they do not provide the prescription to solve the problem. Kohn-Sham *ansatz* is the recipe for replacing the original many-body problem with a more accessible auxiliary independent-particle problem [2, 3, 4].

The Hamiltonian for the auxiliary system is given by

$$\hat{H}_{\text{aux}} = -\frac{1}{2}\nabla^2 + V_{\sigma}(\vec{r}), \quad (2.1)$$

where σ denotes the spin degree of freedom and the Hartree atomic units are used. The ground state density of the independent-particle system is

$$n(\vec{r}) = \sum_{\sigma} \sum_i^{N_{\sigma}} |\psi_{i\sigma}(\vec{r})|^2, \quad (2.2)$$

and the kinetic energy is given by

$$T_{\text{s}}[n] = -\frac{1}{2} \sum_{\sigma} \sum_i^{N_{\sigma}} \langle \psi_{i\sigma}(\vec{r}) | \nabla^2 | \psi_{i\sigma}(\vec{r}) \rangle. \quad (2.3)$$

The classical electrostatic energy (Hartree energy) is defined by

$$E_{\text{H}}[n] = \frac{1}{2} \int \int d\vec{r} d\vec{r}' \frac{n(\vec{r})n(\vec{r}')}{|\vec{r} - \vec{r}'|}. \quad (2.4)$$

The orbitals $\psi_{i\sigma}(\vec{r})$ are the eigenfunctions of the single-particle Hamiltonian for the auxiliary system (Eq. 2.1).

Then, the total energy functional becomes

$$E_{\text{KS}}[n] = T_{\text{s}}[n] + \int d\vec{r} n(\vec{r})V_{\text{ext}}(\vec{r}) + E_{\text{H}}[n] + E_{\text{xc}}[n]. \quad (2.5)$$

Note that the exchange-correlation term $E_{\text{xc}}[n]$ includes the kinetic correlation

omitted in T_s , i.e.,

$$E_{\text{xc}}[n] = F[n] - T_s[n] - E_{\text{H}}[n] \quad (2.6)$$

$$= \langle \hat{T} \rangle - T_s[n] + \langle \hat{U}_{ee} \rangle - E_{\text{H}}[n], \quad (2.7)$$

where the functional $F[n]$ contains the kinetic and interaction energies

$$F[n] = \langle \Psi[n] | \hat{T} + \hat{U}_{ee} | \Psi[n] \rangle. \quad (2.8)$$

From the variational principle, we obtain the Kohn-Sham equation

$$(H_{\sigma}^{\text{KS}} - \varepsilon_{i\sigma})\psi_{i\sigma}(\vec{r}) = 0 \quad (2.9)$$

which can be solved self-consistently. Here,

$$H_{\sigma}^{\text{KS}}(\vec{r}) = -\frac{1}{2}\nabla^2 + V_{\sigma}^{\text{KS}}(\vec{r}) \quad (2.10)$$

$$= -\frac{1}{2}\nabla^2 + V_{\text{ext}}(\vec{r}) + V_{\text{H}}(\vec{r}) + V_{\text{xc},\sigma}(\vec{r}) \quad (2.11)$$

with

$$V_{\text{H}}(\vec{r}) = \frac{\delta E_{\text{H}}}{\delta n(\vec{r}, \sigma)} \quad (2.12)$$

and

$$V_{\text{xc},\sigma}(\vec{r}) = \frac{\delta E_{\text{xc}}}{\delta n(\vec{r}, \sigma)}. \quad (2.13)$$

If we knew the functional $E_{\text{xc}}[n]$, the ground state energy and density can be found. In practice, an approximate form for $E_{\text{xc}}[n]$ is used, which provides

a practically accessible way to calculate the physical properties of the system.

2.1.2 Exchange-correlation functional

In this part, we discuss the exchange-correlation functionals in practical DFT calculations [2, 3, 4].

The simplest approach to describe the exchange and correlation energy would be using that of the homogeneous gas corresponding to the density at each point, which is called the local density approximation (LDA). The exchange-correlation energy in LDA can be written as

$$E_{xc}^{\text{LDA}}[n] = \int d\vec{r} \epsilon_{xc}^h[n(\vec{r})]n(\vec{r}) \quad (2.14)$$

$$= \int d\vec{r} \{ \epsilon_x^h[n(\vec{r})] + \epsilon_c^h[n(\vec{r})] \} n(\vec{r}), \quad (2.15)$$

where the superscript ‘h’ implies the homogeneous electron gas and the exchange and correlation parts are separately written in the final form. (In local spin density approximation (LSDA), we have

$$E_{xc}^{\text{LDA}}[n_\uparrow, n_\downarrow] = \int d\vec{r} \epsilon_{xc}^h[n_\uparrow(\vec{r}), n_\downarrow(\vec{r})]n(\vec{r}) \quad (2.16)$$

$$= \int d\vec{r} \{ \epsilon_x^h[n_\uparrow(\vec{r}), n_\downarrow(\vec{r})] + \epsilon_c^h[n_\uparrow(\vec{r}), n_\downarrow(\vec{r})] \} n(\vec{r}), \quad (2.17)$$

with the spin densities n_\uparrow and n_\downarrow .) The exchange energy of the homogeneous gas is given by

$$E_x[n] = -\frac{3}{4} \left(\frac{3}{\pi} \right)^{\frac{1}{3}} n^{\frac{1}{3}}. \quad (2.18)$$

The correlation energy of the homogeneous gas was calculated accurately using the quantum Monte Carlo methods by Ceperley and Alder [5].

The first step to improve the local approximation would be to include the gradient of the density. But the inclusion of such terms does not give systematic improvement of the local approximation. The generalized gradient approximation (GGA) refers to the functionals that modify the behavior of the gradient terms to maintain the desired properties. The general form of the GGA functional can be written as

$$\begin{aligned} E_{\text{xc}}^{\text{GGA}}[n] &= \int d\vec{r} \epsilon_{\text{xc}}[n, \nabla n, \dots]n(\vec{r}) \\ &= \int d\vec{r} \epsilon_{\text{xc}}^{\text{h}}[n]F_{\text{xc}}[n, \nabla n, \dots]n(\vec{r}). \end{aligned} \quad (2.19)$$

(Including the spin degree of freedom, we have

$$\begin{aligned} E_{\text{xc}}^{\text{GGA}}[n_{\uparrow}, n_{\downarrow}] &= \int d\vec{r} \epsilon_{\text{xc}}[n_{\uparrow}, n_{\downarrow}, \nabla n_{\uparrow}, \nabla n_{\downarrow}, \dots]n(\vec{r}) \\ &= \int d\vec{r} \epsilon_{\text{xc}}^{\text{h}}[n]F_{\text{xc}}[n_{\uparrow}, n_{\downarrow}, \nabla n_{\uparrow}, \nabla n_{\downarrow}, \dots]n(\vec{r}), \end{aligned} \quad (2.20)$$

where n_{\uparrow} and n_{\downarrow} are the spin densities.) There are many versions of GGA. The PBE (Perdew-Burke-Ernzerhof) functional [6, 7] is one of the GGA functionals that are widely used. For the exchange part of the PBE functional, the expression

$$F_{\text{x}}[s] = 1 + \kappa - \frac{\kappa}{1 + \mu s^2/\kappa} \quad (2.21)$$

is used where $s = \frac{|\nabla n|}{2k_{\text{F}}\rho}$ is the dimensionless density gradient, $\mu = 0.21951$, and

$\kappa = 0.804$. The correlation energy of the PBE functional has the form

$$E_c^{\text{GGA}} = \int d\vec{r} [\epsilon_c^h(n, \zeta) + H(n, \zeta, t)]n(\vec{r}), \quad (2.22)$$

with

$$H(n, \zeta, t) = \frac{e^2}{a_0} \gamma \phi^3 \ln \left[1 + \frac{\beta}{\gamma} t^2 \left\{ \frac{1 + At^2}{1 + At^2 + A^2 t^4} \right\} \right], \quad (2.23)$$

where $\beta = 0.066725$, $\gamma = (1 - \ln 2)/\pi^2 = 0.031091$, $\zeta = (n_\uparrow - n_\downarrow)/n$ is the relative spin polarization, $t = |\nabla n|/2\phi k_s n$ is a dimensionless density gradient, k_s is the Thomas-Fermi screening wave number, ϕ is a spin-scaling factor given by

$$\phi(\zeta) = \frac{(1 + \zeta)^{2/3} + (1 - \zeta)^{2/3}}{2}, \quad (2.24)$$

and the function A is written as

$$A = \frac{\beta}{\gamma} \left[\exp \left\{ -\frac{\epsilon_c^h}{\gamma \phi^3 e^2 / a_0} \right\} - 1 \right]^{-1}. \quad (2.25)$$

The PBE functional is theoretically satisfactory in that it fulfills many of the conditions for the exchange-correlation hole and does not have fitting parameters. There are also revised versions of PBE [8, 9].

2.2 Spin-orbit coupling

2.2.1 Noncollinear spin

In general, the spin degree of freedom couples to the spatial one and the direction of the spin axis can vary spatially [3, 10]. To describe the noncollinear case, the spin density matrix is defined as

$$n_{\alpha\beta}(\vec{r}) = \sum_i f_i \psi_{i\alpha}^*(\vec{r}) \psi_{i\beta}(\vec{r}), \quad (2.26)$$

and the Kohn-Sham equation is written as

$$\sum_{\sigma'} (H_{\sigma\sigma'}^{\text{KS}} - \varepsilon_i \delta_{\sigma\sigma'}) \psi_{i\sigma'}(\vec{r}) = 0, \quad (2.27)$$

with

$$H_{\alpha\beta}^{\text{KS}} = -\frac{1}{2} \nabla^2 \delta_{\alpha\beta} + V_{\alpha\beta}^{\text{KS}}(\vec{r}). \quad (2.28)$$

Because the spin-orbit coupling couples the spin to the crystal structure, the noncollinear spin formalism should be considered to include the spin-orbit coupling effect.

2.2.2 Relativistic equation and spin-orbit coupling

In this part, we discuss the spin-orbit coupling [3]. Because the spin-orbit coupling is a relativistic effect, we start from the Dirac equation [11, 12]

$$i\hbar \frac{\partial}{\partial t} \Psi(\vec{r}, t) = (c\vec{\alpha} \cdot \vec{p} + \beta mc^2 + V) \Psi(\vec{r}, t), \quad (2.29)$$

where α and β are given by

$$\alpha_i = \begin{pmatrix} 0 & \sigma_i \\ \sigma_i & 0 \end{pmatrix}, \quad (2.30)$$

and

$$\beta = \begin{pmatrix} I_{2 \times 2} & 0 \\ 0 & -I_{2 \times 2} \end{pmatrix}. \quad (2.31)$$

Here, $\Psi(\vec{r}, t)$ is a 4-component wavefunction and σ_i are the Pauli matrices. (The Dirac equation can be also written in a relativistically covariant form [13].)

If we write the solution of the Dirac equation as

$$\Psi(\vec{r}, t) = \exp(-i\varepsilon t/\hbar) \begin{pmatrix} \phi(\vec{r}) \\ \chi(\vec{r}) \end{pmatrix}, \quad (2.32)$$

we obtain coupled equations

$$\begin{aligned} (\varepsilon - V - mc^2)\phi(\vec{r}) - c(\vec{\sigma} \cdot \vec{p})\chi(\vec{r}) &= 0, \\ (\varepsilon - V + mc^2)\chi(\vec{r}) - c(\vec{\sigma} \cdot \vec{p})\phi(\vec{r}) &= 0, \end{aligned} \quad (2.33)$$

where ϕ and χ are the large and small components, respectively in the case of electrons. For a spherical potential $V(r)$, the wavefunction can be written as [13]

$$\Psi_{njm_j l} = \begin{pmatrix} g_{nj}(r)\varphi_{jm_j l} \\ if_{nj}(r)(\vec{\sigma} \cdot \hat{r})\varphi_{jm_j l} \end{pmatrix} \quad (2.34)$$

using the parity and total angular momentum conservation, in which the total angular momentum is represented by the quantum numbers jm_j , n is the

principal quantum number, and $l = j \pm 1/2$. Here, the function φ_{jm_jl} is

$$\varphi_{jm_jl} = \begin{pmatrix} \sqrt{\frac{l+\frac{1}{2}+m_j}{2l+1}} Y_{l,m_j-\frac{1}{2}} \\ \sqrt{\frac{l+\frac{1}{2}-m_j}{2l+1}} Y_{l,m_j+\frac{1}{2}} \end{pmatrix} \text{ for } j = l + \frac{1}{2}, \quad (2.35)$$

and

$$\varphi_{jm_jl} = \begin{pmatrix} \sqrt{\frac{l+\frac{1}{2}-m_j}{2l+1}} Y_{l,m_j-\frac{1}{2}} \\ -\sqrt{\frac{l+\frac{1}{2}+m_j}{2l+1}} Y_{l,m_j+\frac{1}{2}} \end{pmatrix} \text{ for } j = l - \frac{1}{2}, \quad (2.36)$$

where $Y_{l,m}$ are the spherical harmonics. Then, we obtain [3]

$$\begin{aligned} & -\frac{\hbar^2}{2M(r)} \frac{1}{r^2} \frac{d}{dr} \left(r^2 \frac{dg_{n\kappa}(r)}{dr} \right) + \left[V(r) + \frac{\hbar^2}{2M(r)} \frac{\kappa(\kappa+1)}{r^2} \right] g_{n\kappa}(r) \\ & - \frac{\hbar^2}{4\{M(r)\}^2 c^2} \frac{dV(r)}{dr} \frac{dg_{n\kappa}(r)}{dr} - \frac{\hbar^2}{4\{M(r)\}^2 c^2} \frac{dV(r)}{dr} \frac{1+\kappa}{r} g_{n\kappa}(r) \\ & = (\varepsilon - mc^2) g_{n\kappa}(r), \end{aligned} \quad (2.37)$$

where

$$M(r) = m + \frac{1}{2c^2} [\varepsilon - mc^2 - V(r)], \quad (2.38)$$

and κ is defined as $\kappa = j + \frac{1}{2} = l$ for $l = j + \frac{1}{2}$ and $\kappa = -(j + \frac{1}{2}) = -(l+1)$ for $l = j - \frac{1}{2}$. The last term on the left-hand side of Eq. 2.37 corresponds to the spin-orbit coupling. Note that the spin-orbit Hamiltonian can be expressed as

$$H_{\text{spin-orbit}} = \frac{1}{2M^2 c^2} \frac{1}{r} \frac{dV}{dr} \vec{L} \cdot \vec{S}, \quad (2.39)$$

where \vec{L} is the orbital angular momentum and \vec{S} is the spin angular momentum.

Because the relativistic effects originate from the deep interior region near

the nucleus, their effect on the valence electrons can be incorporated in the pseudopotentials. The relativistic effects can be included by generating j -dependent pseudopotentials ($j = l + 1/2$ and $j = l - 1/2$ for $l > 0$, and $j = 0 + 1/2$ for $l = 0$) from the large component solutions of the Dirac equation [14, 15]. After a fully relativistic all-electron calculation for a single atom is performed, a pseudopotential V_j for each j is found, where the Kohn-Sham equation for V_j has solutions that match the large component solutions of the Dirac equation. The total ionic pseudopotential is given as [14]

$$V_{\text{ps}} = \sum_{l,m} \left| \varphi_{l+\frac{1}{2},m+\frac{1}{2},l} \right\rangle V_{l+\frac{1}{2}} \left\langle \varphi_{l+\frac{1}{2},m+\frac{1}{2},l} \right| + \left| \varphi_{l-\frac{1}{2},m-\frac{1}{2},l} \right\rangle V_{l-\frac{1}{2}} \left\langle \varphi_{l-\frac{1}{2},m-\frac{1}{2},l} \right|. \quad (2.40)$$

The pseudopotential can be written as the sum of a local part and a short-ranged nonlocal part, and the nonlocal part can be written as the computationally efficient fully separable Kleinman-Bylander form [18]. In the case with the spin-orbit coupling, we have the form [3, 19, 18]

$$V_{j=l\pm 1/2}^{\text{NL}} = \sum_{l,m} \frac{\left| \delta V_{l\pm 1/2} \psi_{l\pm 1/2,m}^{\text{ps}} \right\rangle \left\langle \psi_{l\pm 1/2,m}^{\text{ps}} \delta V_{l\pm 1/2} \right|}{\left\langle \psi_{l\pm 1/2,m}^{\text{ps}} \left| \delta V_{l\pm 1/2} \right| \psi_{l\pm 1/2,m}^{\text{ps}} \right\rangle}. \quad (2.41)$$

Also, we can define an averaged potential including the scalar relativistic effects [3, 16, 17]

$$V_l = \frac{1}{2l+1} \{ (l+1)V_{l+1/2} + lV_{l-1/2} \} \quad (2.42)$$

(Note that the only term depending on the two cases $j = l + 1/2$ and $j = l - 1/2$

in Eq. 2.37 is the spin-orbit term, which can be removed by weighted average.), and the spin-orbit coupling effect is included in

$$V_l^{\text{SO}} = \frac{2}{2l+1} \{V_{l+1/2} - V_{l-1/2}\}, \quad (2.43)$$

and the total ionic pseudopotential can be expressed as

$$V_{\text{ps}} = \sum_l |l\rangle (V_l + V_l^{\text{SO}} \vec{L} \cdot \vec{S}) \langle l| \quad (2.44)$$

in this case. The Kohn-Sham equation with the relativistic effects can be solved directly in the two-component spinor space, or the perturbative approach can be used where the effect of the spin-orbit coupling is included through a second variational step on the scalar relativistic result [19, 20, 21, 22].

Chapter 3

Topological insulators

3.1 Topological phase transitions in Sb_2Te_3 thin films by external electric fields

3.1.1 Introduction

The first appearance of the topological phases in condensed matter physics is the quantum Hall effect [23, 24]. In the quantum Hall system, the existence of conducting chiral edge states are attributed to the nontrivial topology represented by the Chern number, where the time reversal symmetry is broken by external magnetic fields. Recently, it was found that the time reversal invariant version can be defined, called a topological insulator (TI), and the corresponding topological invariants are \mathbb{Z}_2 invariants [25, 26]. There have been theoretical and experimental studies for both two-dimensional (2D) and three-dimensional (3D) TIs [27, 28]. (A 2D TI is also called a quantum spin Hall system.) Topological insulators also possess topological boundary states,

which are guaranteed to exist as long as the time reversal symmetry is kept. Because the topological boundary states provide robust conducting channels, the control of the boundary states would be useful for nano-device applications.

The topological phases of materials depend on various parameters of the system; for example, lattice constants affect the topological phases [29] and a topological quantum phase transition can be driven by applying pressure. Here, we consider an external electric field [25, 30] as an another possible parameter that can drive topological phase transitions in 2D systems. 2D TIs have robust edge states protected by the time reversal symmetry whereas normal insulators (NIs) may have trivial edge states. Thus, topological phase transitions using external fields can be considered as practically convenient way to manipulate the conducting edge states.

We choose thin films of 3D TIs as our system to demonstrate the phase transitions by the external fields. The thin films of 3D TIs can have different band topology according to the thicknesses of the films due to the band inversions between the subbands [31]. Thus it is convenient to demonstrate the phase transitions from a NI to a TI and vice versa, starting from different layer thicknesses. It is to be noted that the first model (Kane-Mele model) study for a 2D TI considered the topological phases varying the Rashba term that describes the effect of perpendicular electric fields or interaction with a substrate [25]. Also, there is a numerical study in CdTe/HgCdTe/CdTe quantum wells to show the topological phase transitions by electric fields [30].

In this section, we present first-principles calculations based on density functional theory to show that topological phase transitions both from a NI to

a TI and from a TI to a NI can be driven by external electric fields in thin films of Sb_2Te_3 [32]. We find that the band topology of Sb_2Te_3 thin films depends on the thicknesses of the films and 3 quintuple layers (QLs) is a 2D NI whereas 4 QLs is a 2D TI. It is shown that 3 QLs of Sb_2Te_3 can be transformed from a NI to a TI by external fields. In the case of 4 QLs, it is possible to drive the topological phase transition from a TI to a NI. The \mathbb{Z}_2 topological invariant ν is calculated to verify the 2D bulk band topology ($\nu = 1$ for a TI, $\nu = 0$ for a NI) using the lattice computation method of the \mathbb{Z}_2 invariant [33, 34]. Also, the edge state configurations are depicted to confirm the band topology, where the edge states of semi-infinite 2D thin films are obtained by the Green function method [35, 36].

3.1.2 Results and Discussion

Sb_2Te_3 is known to be a 3D strong TI that has a single surface Dirac cone in the (111) surface [37]. The symmetry of the atomic structure is rhombohedral with the space group $R\bar{3}m$ (No. 166). It is a layered structure, where five layers (Te-Sb-Te-Sb-Te) form a unit, called a QL (Fig. 3.1). Whereas covalent bonding is important within a QL van der Waals interaction is dominant between QLs, hence the material can be dealt with in units of QLs in practice. Because Sb_2Te_3 is a 3D TI there appear surface Dirac cones in the upper and lower surfaces if a film of the material is formed. When the film thickness is thin, the inter-surface interaction opens a small gap in the band structure (Fig. 3.2). Thus the thin films of Sb_2Te_3 are 2D insulators (gapped systems) and we consider the bulk band topology of them. (The surface states are considered

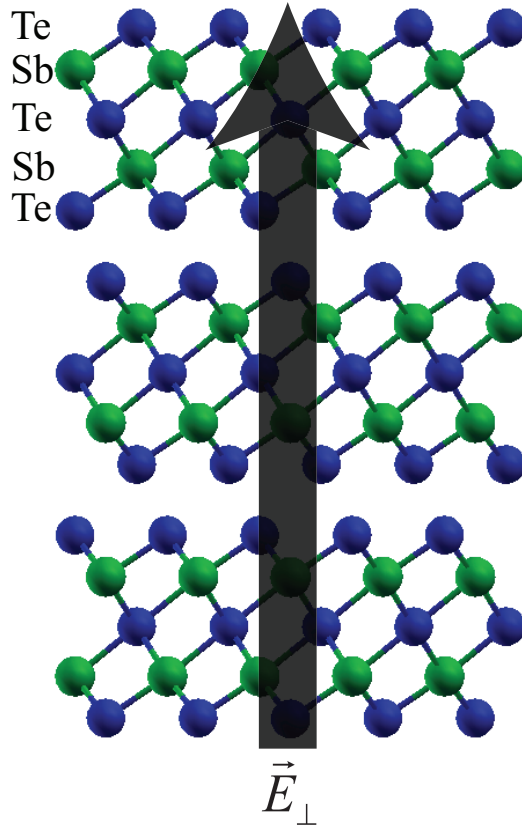


Figure 3.1: Atomic structure of Sb₂Te₃ 3QLs with a schematic illustration of the external electric field.

to be 2D bulk states as opposed to edge states of the 2D system.) The gap sizes of 3 and 4 QLs are calculated to be 9 and 14 meV, respectively.

In the case of a centrosymmetric system, the \mathbb{Z}_2 invariants can be calculated from the wavefunction parities at the time reversal invariant momenta (TRIM) [38]. But the inversion symmetry is broken by external fields in our case, and we need a more general method to calculate the \mathbb{Z}_2 invariants. For this purpose, we adopt the lattice computation method of the \mathbb{Z}_2 invari-

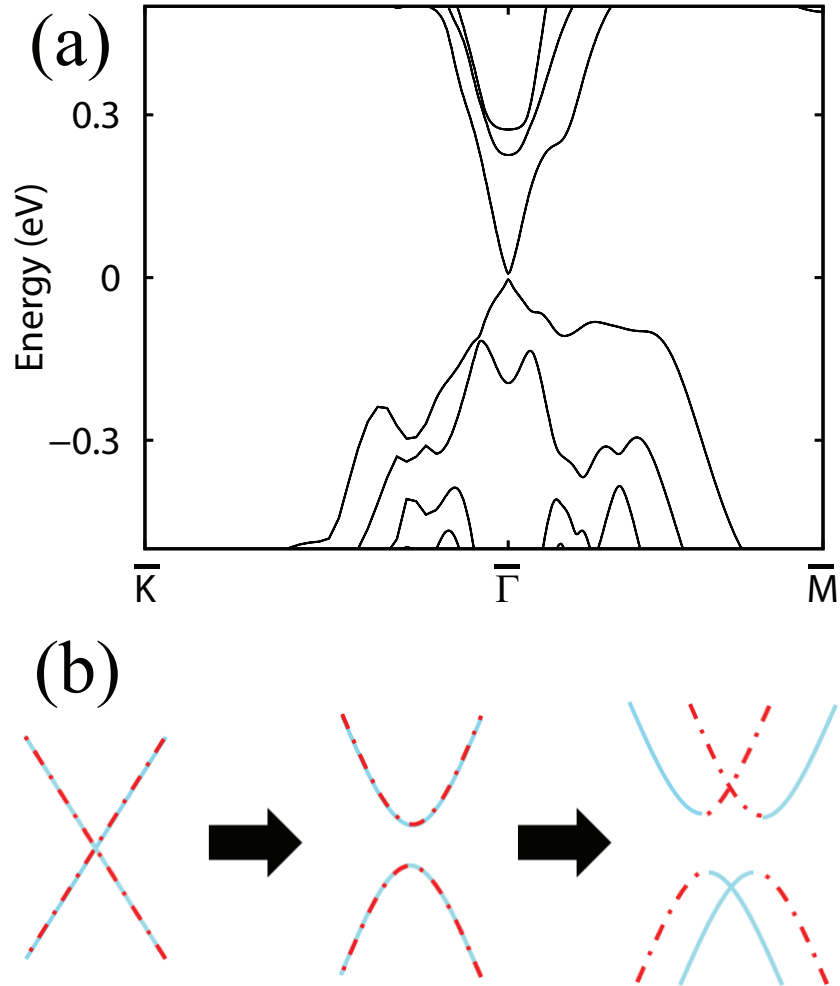


Figure 3.2: Electronic band structures of Sb_2Te_3 thin films. (a) The band structure of Sb_2Te_3 3QLs near the Fermi energy. (b) Schematics for the band structure. The topological surface states (Dirac cones) of upper and lower surfaces (left) are present. The intersurface interaction opens a small energy gap (center). The external electric fields breaks the inversion symmetry (right).

ants [33, 34]. The \mathbb{Z}_2 invariant can be written as the integration form [39]

$$\nu = \frac{1}{2\pi} \left(\oint_{\partial B^-} \mathcal{A} \cdot d\mathbf{k} - \int_{B^-} \mathcal{F} d^2k \right) \text{ mod } 2. \quad (3.1)$$

(\mathcal{A} and \mathcal{F} represent Berry connection and Berry curvature respectively, and half the BZ is denoted by B^- .) In the lattice computation method, the expression is evaluated in a discretized BZ. The Berry connection \mathcal{A} and Berry curvature \mathcal{F} in the lattice BZ is given by [40, 33, 34]

$$\mathcal{A}_\mu(\mathbf{k}_j) = \text{Im} \log U_\mu(\mathbf{k}_j), \quad (3.2)$$

$$\mathcal{F}(\mathbf{k}_j) = \text{Im} \log U_1(\mathbf{k}_j)U_2(\mathbf{k}_j + \mathbf{e}_1)U_1^{-1}(\mathbf{k}_j + \mathbf{e}_2)U_2^{-1}(\mathbf{k}_j), \quad (3.3)$$

with the link variable U defined by

$$U_\mu(\mathbf{k}_j) = \det [\langle u_n(\mathbf{k}_j) | u_m(\mathbf{k}_j + \mathbf{e}_\mu) \rangle], \quad (3.4)$$

where \mathbf{e}_μ denotes the unit vector on the k -mesh. Then an integer field $n(\mathbf{k}_j)$ is defined at each plaquette by

$$n(\mathbf{k}_j) = \frac{1}{2\pi} [\{\Delta_1 \mathcal{A}_2(\mathbf{k}_j) - \Delta_2 \mathcal{A}_1(\mathbf{k}_j)\} - \mathcal{F}(\mathbf{k}_j)]. \quad (3.5)$$

The \mathbb{Z}_2 invariant ν is given by the sum of the interger field $n(\mathbf{k}_j)$ in half the BZ modulo 2, i.e.,

$$\nu = \sum_{\mathbf{k}_j \in B^-} n(\mathbf{k}_j) \text{ mod } 2. \quad (3.6)$$

If $\nu = 1$ for occupied bands, the system is a TI. If $\nu = 0$ for occupied bands, the

system is a NI. (Note that the band topology can be defined for each separated band manifold.) In this study, the band topology of occupied p -like bands are considered, because other occupied bands are separated in energy sufficiently. The band topology of thin films of 3D TI can depend on the thicknesses of them due to the band inversion between the electron and hole bands [31]. We find that 1, 2, and 3 QLs of Sb_2Te_3 are 2D NIs and 4, 5, and 6 QLs are 2D TIs. We choose 3 and 4 QLs to demonstrate the topological phase transitions from a NI to a TI and vice versa.

We consider a topological quantum phase transition driven by the external electric field in thin films of Sb_2Te_3 . Here, the external field is an adiabatic parameter that can be considered to change the Hamiltonian continuously. Because the topological invariant assigned to each band manifold is an integer, it is necessary to have a singular point for the integer number to change by the continuous transformation. Actually, the singular behavior appears as a gap closing and two band manifolds (occupied and unoccupied bands) merge together to exchange the topological invariants. The position of the gap closing point in BZ is dependent on the symmetry of the system. In a centrosymmetric system, the gap closing occurs at TRIMs. If the inversion symmetry is broken, the gap closing occurs at points other than TRIMs [41, 42].

The 3QLs of Sb_2Te_3 is a NI and we intend to drive a topological phase transition. Without external fields, the thin films have the inversion symmetry and time reversal symmetry, which keep the spin degeneracy in the entire Brillouin zone (BZ). If external electric fields are applied, the inversion symmetry is broken. Thus, the two-fold spin degeneracy is lifted in general, and Rashba-

type bands appear near the Fermi energy (Fig. 3.2(b)). For $E_{\perp} = 0.03 \text{ V/\AA}$, the band structure shows Rashba-type bands due to the inversion symmetry breaking, but the band topology is still trivial ($\nu = 0$, Fig. 3.3(a)). If we apply stronger fields ($E_{\perp} = 0.15 \text{ V/\AA}$), the system becomes a TI ($\nu = 1$, Fig. 3.3(c)). Between the topologically trivial and nontrivial phases, there should appear the gap closing point as the phase boundary and the critical field strength for the phase transition is estimated to be $0.06 < E_c < 0.075 \text{ V/\AA}$ in 3 QLs. Although the band structure at the exact gap closing point is difficult to obtain numerically, the band structure calculation close to the Fermi energy with the external field near the critical value indicates that the gap closing occurs at a point in the $\bar{\Gamma} - \bar{K}$ direction (Fig. 3.3(b)), which is consistent with the \mathbb{Z}_2 invariant calculations because the gap closing occurs at an odd number of points in half the BZ. In the case of 4 QLs, the phase transition occurs from a TI to a NI. It is found that we have $\nu = 1$ for 4 QLs without the fields, and $\nu = 0$ for $E_{\perp} = 0.2 \text{ V/\AA}$, where the critical field is estimated to be $0.125 < E_c < 0.15 \text{ V/\AA}$. As mentioned above, the 2D bulk band topology is calculated by the lattice computation method. The n-field configurations for 3QLs before and after the phase transition is shown in Fig. 3.4. Although the n-field configuration is gauge-dependent, the sum modulo 2 in half the BZ is not because it is a topological invariant that must be a gauge-independent physical quantity. In our calculation, an arbitrary gauge is used and other choice of the gauge should give the same result for the \mathbb{Z}_2 invariant.

The bulk band topology can be equivalently checked by boundary state configurations. In the case of 2D insulators, a TI has nontrivial edge states

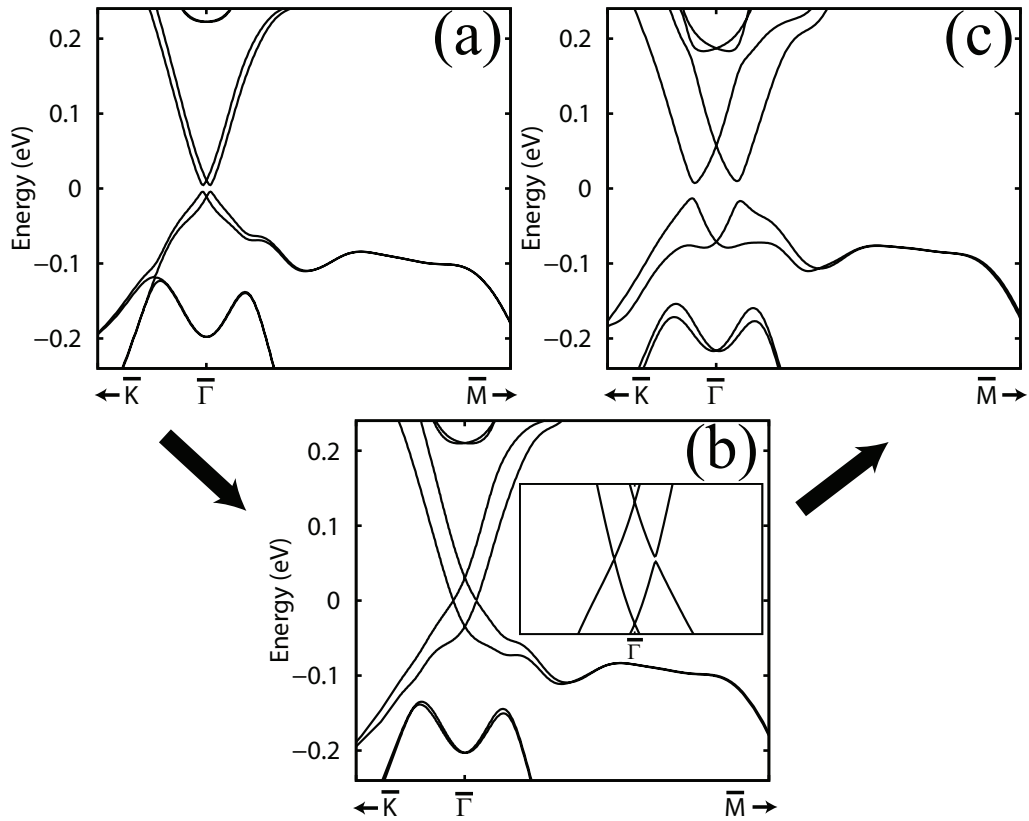


Figure 3.3: Electronic band structures of Sb_2Te_3 3QLs with external fields. The band structures of Sb_2Te_3 3QLs near the Fermi energy are depicted with (a) $E_{\perp} = 0.03 \text{ V/\AA}$, (b) $E_{\perp} = 0.067 \text{ V/\AA}$ (c) $E_{\perp} = 0.15 \text{ V/\AA}$. The inset in (b) shows the band structure close to the Fermi energy.

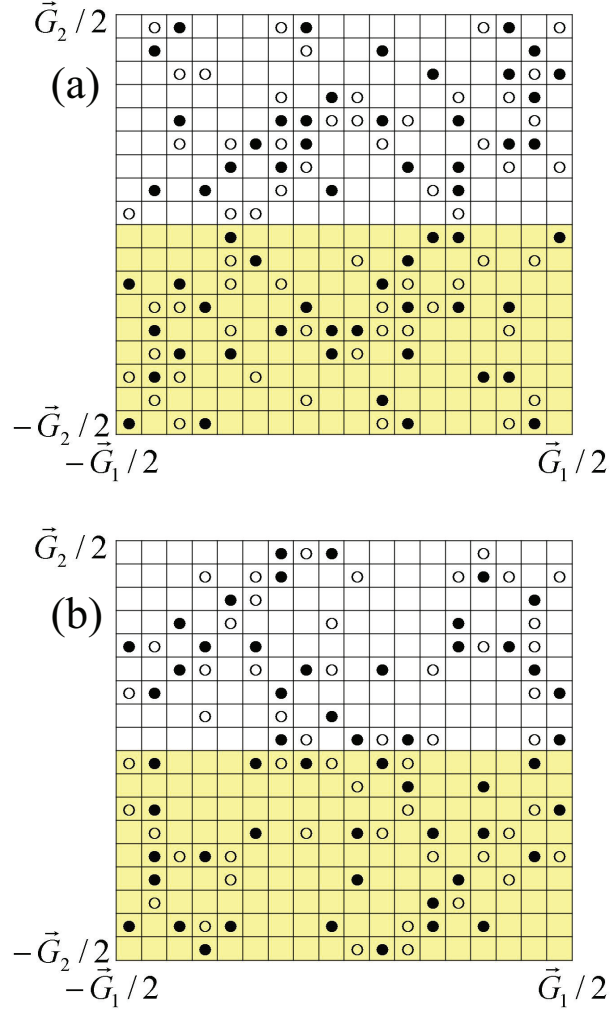


Figure 3.4: The n-field configurations for Sb_2Te_3 3QLs with external fields. The n-field configurations are depicted with (a) $E_\perp = 0.03 \text{ V/\AA}$, (b) $E_\perp = 0.15 \text{ V/\AA}$. The empty circles represent +1 and the filled circles represent -1. The plaquettes with no circles represent 0. The sum of the n-field values in half the BZ (modulo 2) gives the \mathbb{Z}_2 invariant. Thus we have $\nu = 0$ in (a) and $\nu = 1$ in (b).

connecting the conduction and valence bulk bands, whereas a NI has trivial ones. The nontrivial edge states cross the Fermi level odd number of times in half the BZ, whereas the trivial ones do even number of times. The existence of these boundary states can be explained by the following argument. The band topology is the classification by considering the equivalence classes of bulk Hamiltonian that can be continuously deformed into one another without closing the energy gap under the time reversal symmetry [27]. If we imagine the change of the bulk Hamiltonian of a TI when we move to the boundary of the system and finally the vacuum, the energy gap should be closed in between because the two sides of the boundary have different topology (the topology of the vacuum is trivial.). Thus, gapless boundary states should appear when the two sides of the boundary have different band topology.

The edge state dispersion is obtained by using highly convergent schemes for the calculation of bulk and surface Green functions [35, 36]. We construct maximally localized Wannier functions of the system [43, 44] using the results of the density functional theory calculation and obtain the Hamiltonian in terms of the Wannier functions. Then, energy and momentum-dependent local density of states (EMLDOS) in edge and bulk layers are computed by the Green function method. In this method, the edge state dispersion of the semi-infinite 2D film is calculated and the connectivity of the edge and bulk states is clearly demonstrated, which is important for checking the bulk band topology. The edge state configurations of 3 QLs are presented in Fig. 3.5. When the external field is not present, there appear no edge states near the Fermi energy (Fig. 3.5(a)). In contrast, the edge states that connect the bulk conduction and

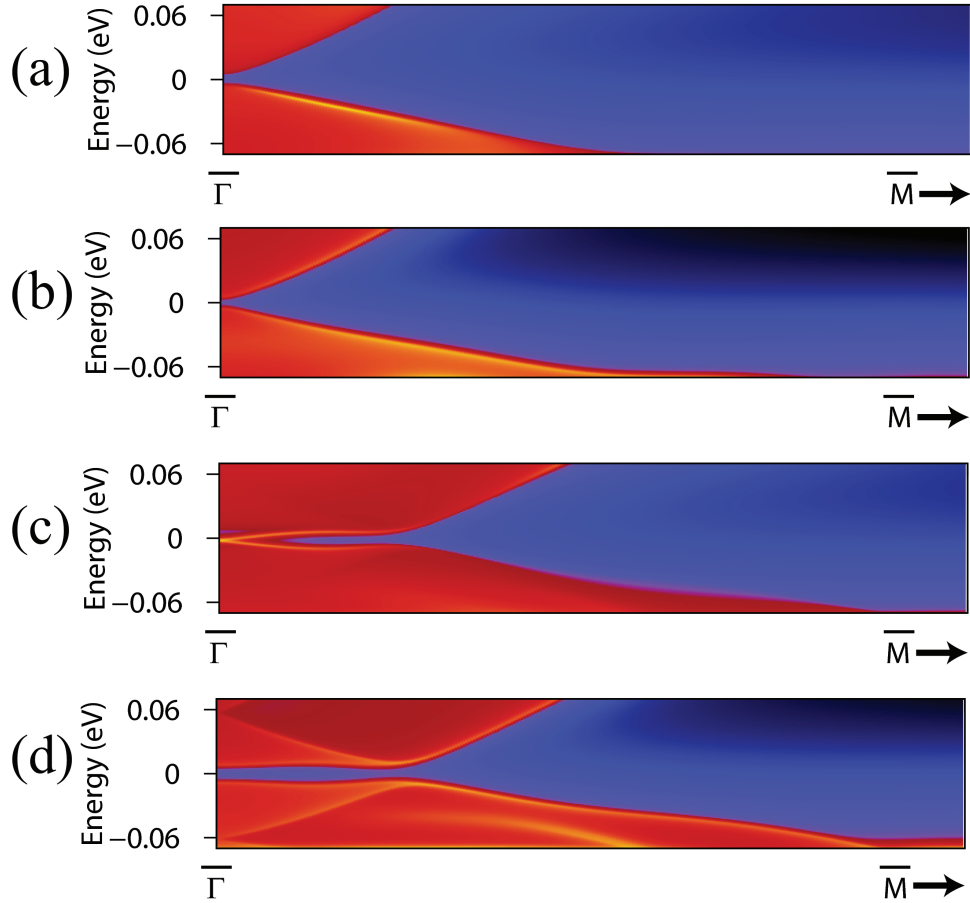


Figure 3.5: The EMLDOS for Sb_2Te_3 3QLs with external fields. The EMLDOS for the edge principal layer are presented with (a) $E_{\perp} = 0.0 \text{ V/\AA}$, (c) $E_{\perp} = 0.15 \text{ V/\AA}$. For comparison, the EMLDOS for the bulk principal layer are presented with (b) $E_{\perp} = 0.0 \text{ V/\AA}$, (d) $E_{\perp} = 0.15 \text{ V/\AA}$. In (c), the topological gapless edge states appear in the bulk energy gap.

valence bands appear when $E_{\perp} = 0.15 \text{ V/\AA}$ (Fig. 3.5(c)). These gapless states are the topological edge states that come from the nontrivial band topology of the thin film with the external fields. It can be confirmed that the gapless states are edge states (not bulk states) by depicting the EMLDOS of bulk layers (Fig. 3.5(d)). The edge state configurations are consistent with the results of our calculations of the \mathbb{Z}_2 invariants.

3.1.3 Conclusions

In conclusion, we demonstrated that topological phase transitions can be driven by external electric fields. It was shown that 3 QDs of Sb_2Te_3 makes a topological quantum phase transition from a NI to a TI by the external electric fields. On the contrary, 4 QDs is a TI without the external fields and becomes a NI by the fields. The 2D bulk band topology is verified by directly calculating the topological \mathbb{Z}_2 invariant. Also, the edge state configurations are found to reflect the bulk band topology. The results suggest that the topological phase transition by external fields might be useful for the realization and control of the topological phases in thin films. The control of topological edge conducting channels would be also important in practical applications.

3.1.4 Methods

Quantum Espresso package was used to calculate the electronic structures [45]. A planewave basis set with the energy cutoff 34 Ry was employed. PBE (Perdew-Burke-Ernzerhof) type exchange-correlation functional was adopted [6]. Fully relativistic pseudopotentials were used to include the effect of the spin-

orbit coupling (SOC). We used the experimental lattice constant of Sb_2Te_3 [46]. The calculation of the \mathbb{Z}_2 invariant was done by using the wavefunctions in discretized BZ [33, 34]. Wannier90 package was used to obtain the Hamiltonian with a localized basis [47] and highly convergent schemes for the calculation of bulk and surface Green functions were employed to calculate the EMLDOS of the semi-infinite 2D system [35, 36].

3.2 Topological narrow bands in Sn-Te bilayers with defect superstructures

3.2.1 Introduction

Topological insulators have the band inversion between conduction and valence bands due to the SOC. Thus a guide to search for a topologically nontrivial material is to choose heavy species with strong SOC strength as the component atoms. In addition, we should have appropriate symmetry and structure to induce the band inversion. In the previous section (Sec. 3.1), it was shown that the external electric fields can be used to realize a TI phase and control the topological edge states. Here, we consider defect superstructures to realize a TI phase in 2D thin films. If we introduce a defect superstructure in a 2D NI, defect-induced narrow (localized) bands appear near the Fermi energy. We will investigate the band topology of the narrow bands expecting that the system becomes a TI due to the nontrivial band topology of the narrow bands. Atomic precision defect superstructures were reported in porous graphene and iron-based superconductors in experiments [48, 49, 50].

We choose a Sn-Te bilayer, which consists of one triangular Sn layer and another triangular Te layer obtained by exfoliating bulk SnTe in the (111) direction, to verify the possibility of having a TI phase due to the defect superstructure. Because SnTe has the SOC that is strong enough to have band inversions between the conduction and valence bands [51, 52], the Sn-Te bilayer is appropriate to test whether the introduction of a simple 2D defect array (for example, a periodic array of vacancies with the triangular symmetry) can induce topologically nontrivial bands near the Fermi energy. We note that there is a theoretical study on possible TI phases in a square lattice with a perfect vacancy superstructure [53].

In this section, we investigate the band topology of the Sn-Te bilayer with defect superstructures [54]. We show that the Sn-Te bilayer becomes a TI if we introduce appropriate periodic defects whereas the pristine Sn-Te bilayer is a NI. Using first-principles calculations based on density functional theory, it is shown that the Sn-Te bilayer with Sn vacancies in 5×5 periodicity is a TI in its natural electron filling and there appear topologically nontrivial narrow bands (TNNBs) near the Fermi energy. We find that without the SOC there appear degenerate defect-induced bands due to the crystal symmetry and the topologically nontrivial character originates from the topologically nontrivial spin-orbit splitting of the defect bands. Due to the narrow band width of the topological bands, we further show that the system can be driven to a NI phase by charge doping, which would be a useful way for the control of topological edge states by the gate voltage in practice. The band topology is calculated by using the lattice computation method of the \mathbb{Z}_2 invariant in a

discretized BZ [33, 34]. The dispersion of the edge states is calculated by the Green function method [35, 36], and the topological character of the narrow bands is confirmed. In addition, the bilayer with Te vacancy array (in 5×5 periodicity) can be made to be a TI if neighboring Sn atoms are replaced by Sb atoms and one hole is doped per cell. Topological phase transition by charge doping is also possible in the Te vacancy case.

3.2.2 Results and Discussion

SnTe is known to be a topological crystalline insulator [51, 52]. The bulk Hamiltonian of SnTe shows band inversions between the conduction and valence bands with respect to that of PbTe [55]. However, the band inversion occurs at four L points of the BZ resulting in trivial band topology of occupied bands in the TI sense. The band topology of a 3D insulator is represented by four \mathbb{Z}_2 invariants $(\nu_0; \nu_1\nu_2\nu_3)$, where ν_0 is the strong invariant and ν_1, ν_2, ν_3 are the weak invariants. Our calculation gives the \mathbb{Z}_2 invariants $(\nu_0; \nu_1\nu_2\nu_3) = (0; 000)$, hence SnTe is a NI. SnTe has a rocksalt structure (the space group $Fm\bar{3}m$, No. 225) at the room temperature. Because the face-centered cubic structure is the cubic close-packed structure, it can be viewed as stacking of 2D triangular lattices of Sn and Te alternately. At low temperature (below 100 K), SnTe undergoes a structural phase transition from the cubic structure to a rhombohedral structure with a small dimerization along (111) direction [56]. Thus, the Sn-Te bilayer is a natural unit if the rhombohedral distortion occurs. One of the advantages of taking Sn-Te bilayer as our model system is that it is convenient to introduce a simple triangular defect

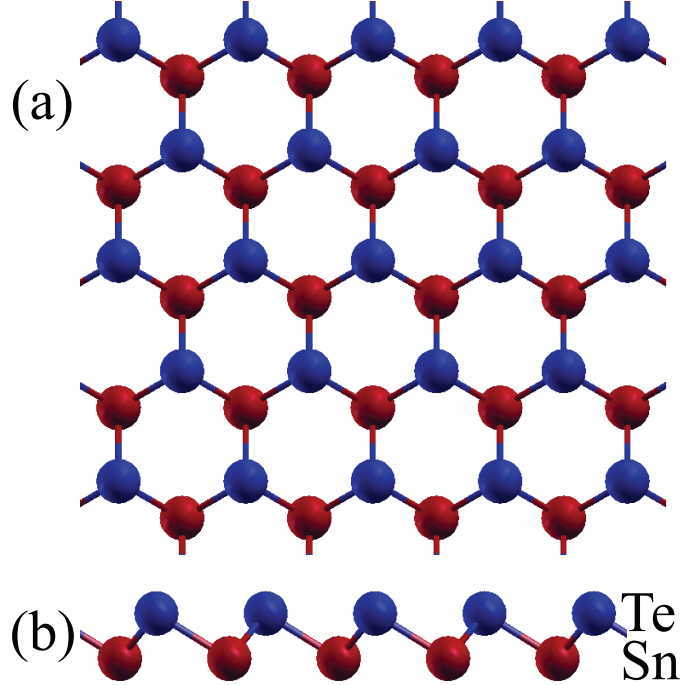


Figure 3.6: Atomic structure of a Sn-Te bilayer. (a) Top view. (b) Side view. The Sn-Te bilayer forms a buckled honeycomb structure.

array with strong enough SOC. The atomic structure (Fig. 3.6) is a buckled honeycomb structure with two atomic layers of a single species (Sn and Te). In terms of the electronic structure, the Sn-Te bilayer is an insulator and the energy gap is estimated to be $\simeq 1.1$ eV (Fig. 3.7). We calculate the \mathbb{Z}_2 invariant and the result is $\nu = 0$, thus the Sn-Te bilayer is a 2D NI.

We want to realize a TI phase by introducing a defect superstructure to the Sn-Te bilayer. We first explain our scenario for a 2D TI phase induced by a defect superstructure. When defects (for example, vacancies) form a periodic array, defect-induced bands appear near the Fermi energy in general. The defect-induced narrow (localized) bands can be degenerate without SOC if the

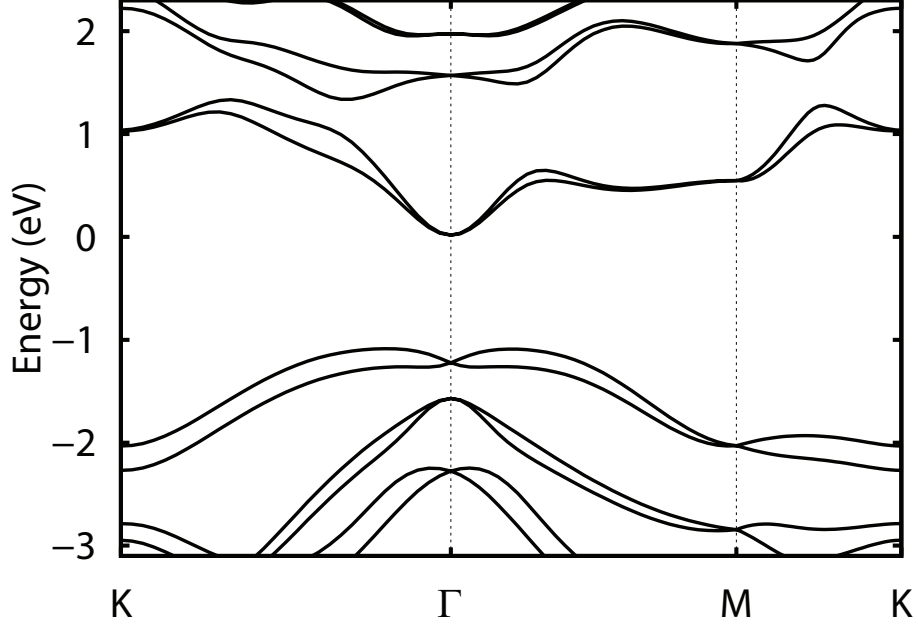


Figure 3.7: Electronic band structure of a Sn-Te bilayer.

crystal symmetry of the superstructure is sufficiently high (Fig. 3.8(a)). Now the SOC can split off the degenerate bands and if the splitting occurs in a topologically nontrivial way the resultant split bands are TNNBs with $\nu = 1$. Because the band topology of the system is determined by the sum (modulo 2) of the \mathbb{Z}_2 invariants of occupied bands, the system becomes a 2D TI with $\nu = 1$ and will have topological edge states at the Fermi energy (Fig. 3.8(b)). Also, due to the narrow band width of the TNNBs, it is possible to have a topological phase transition from a TI to a NI by charge doping. If electrons are doped to set the Fermi level above the upper TNNBs, the 2D system becomes a NI with $\nu = 0$ (Fig. 3.8(c)). If holes are doped to set the Fermi level below the lower TNNBs, the system also becomes a NI (Fig. 3.8(d)).

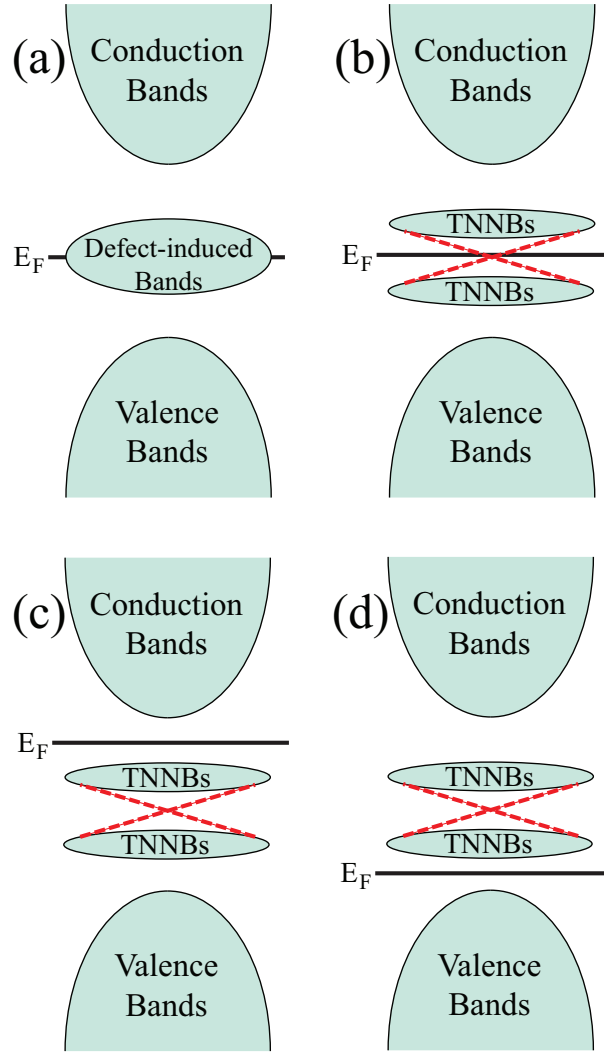


Figure 3.8: Schematic illustration of topologically nontrivial narrow bands induced by the defect superstructure. (a) Defect-induced degenerate bands appear at the Fermi level (without SOC). (b) Topologically nontrivial narrow bands appear due to the spin-orbit splitting. (c) Electron doping case. (d) Hole doping case.

As an example of the above scenario, we consider the Sn-Te bilayer with Sn vacancies with 5×5 periodicity (Fig. 3.9). We perform first-principles density functional theory calculations to obtain the band structure. A Sn vacancy leaves dangling bond states of nearby Te atoms that would appear near the Fermi energy in the electronic band structure. If the SOC is not included in the calculations, the crystal symmetry protects the double (except for the spin) degeneracy of the defect-induced bands at the Γ point of the BZ that belongs to the 2D representation E of the point group C_{3v} , where the Fermi level lies in the defect-induced bands (Fig. 3.10(c)). When we include the effect of the SOC, the double group representation allows the degeneracy lift by the spin-orbit splitting. The dispersion of those defect-induced bands depends on the density of the vacancies. We find that a single vacancy in the 5×5 cell makes an energy gap in the band structure (Fig. 3.10(a),(b)). The gap size is calculated to be $\simeq 12$ meV. If we calculate the \mathbb{Z}_2 invariants of the defect-induced bands using the lattice computation method [33, 34], both the upper and lower bands near the Fermi energy are topologically nontrivial ($\nu = 1$). That is, the spin-orbit splitting of the defect-induced bands occurs in a topologically nontrivial way to have TNNBs above and below the Fermi energy (Fig. 3.10(b)). Thus, the Sn-Te bilayer with the Sn vacancy superstructure is a TI in its natural electron filling. The corresponding n-field configuration for the upper TNNBs is presented in Fig. 3.11(a). Also, the absolute square of the wavefunction of the upper TNNBs at the Γ point of the BZ is presented in Fig. 3.11(b) and we confirm that the states show localized character around the defect site.

Because the band topology is reflected in the dispersion of the boundary

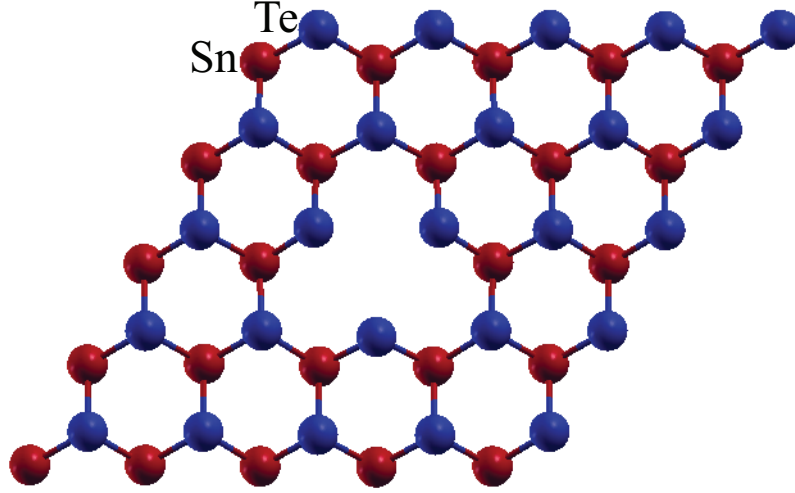


Figure 3.9: Atomic structure of the Sn-Te bilayer with the Sn vacancy superstructure.

(edge) states, we calculate the edge state configurations to confirm the topological character of the system. As in the previous section, we obtained the Hamiltonian in terms of Wannier functions and employed the Green function method [35, 36] to obtain the edge state dispersion of the semi-infinite Sn-Te bilayer. The result is presented in Fig. 3.12. In accord with our \mathbb{Z}_2 invariant calculation, topological gapless edge states appear between the upper and lower TNNBs if we calculate the EMLDOS of the edge layer (Fig. 3.12(a)). For comparison, we also calculate the EMLDOS of the bulk layer (Fig. 3.12(b)) and confirm that the gapless states are indeed edge states (as opposed to bulk states). The topological character of the edge states in Fig. 3.12(a) can be seen by noting that they cross the Fermi level an odd number of times (one time in this case) in half the BZ. (Because of the time reversal symmetry, the dispersion of the edge states in the other half of the BZ can be obtained by

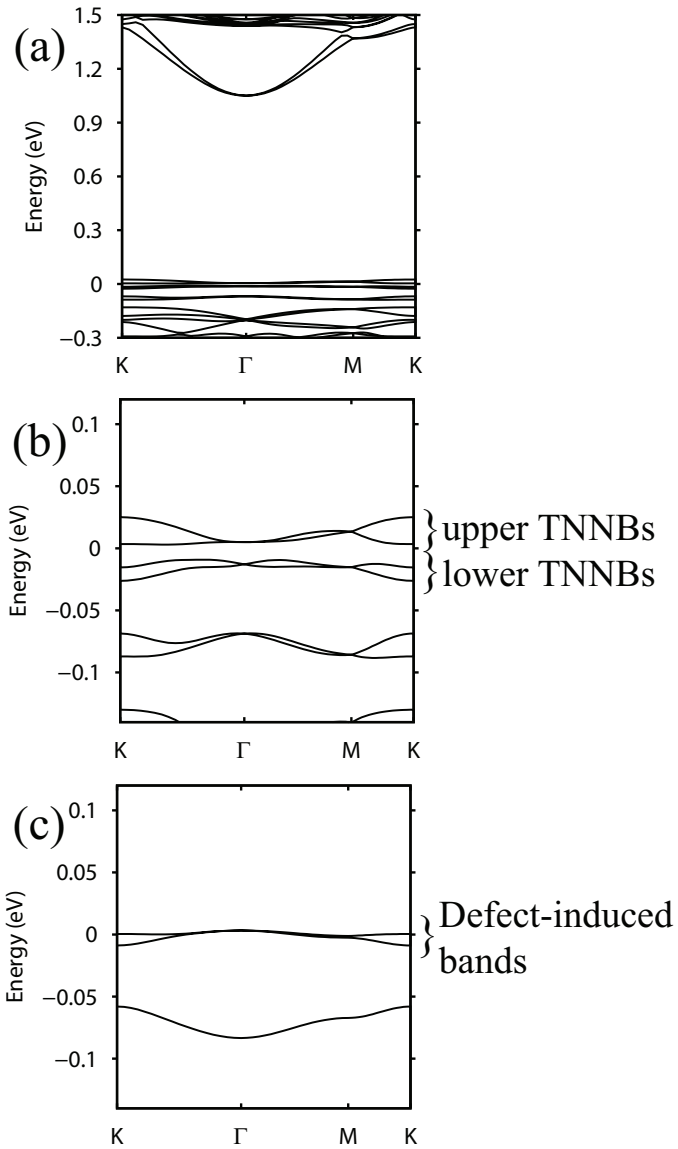


Figure 3.10: Electronic structure of the Sn-Te bilayer with the Sn vacancy superstructure. (a) Band structure of the Sn-Te bilayer with Sn vacancies in 5×5 periodicity. (b) Band structure near the Fermi energy. (c) Band structure near the Fermi energy without SOC. The TNNBs have nontrivial \mathbb{Z}_2 invariants ($\nu = 1$).

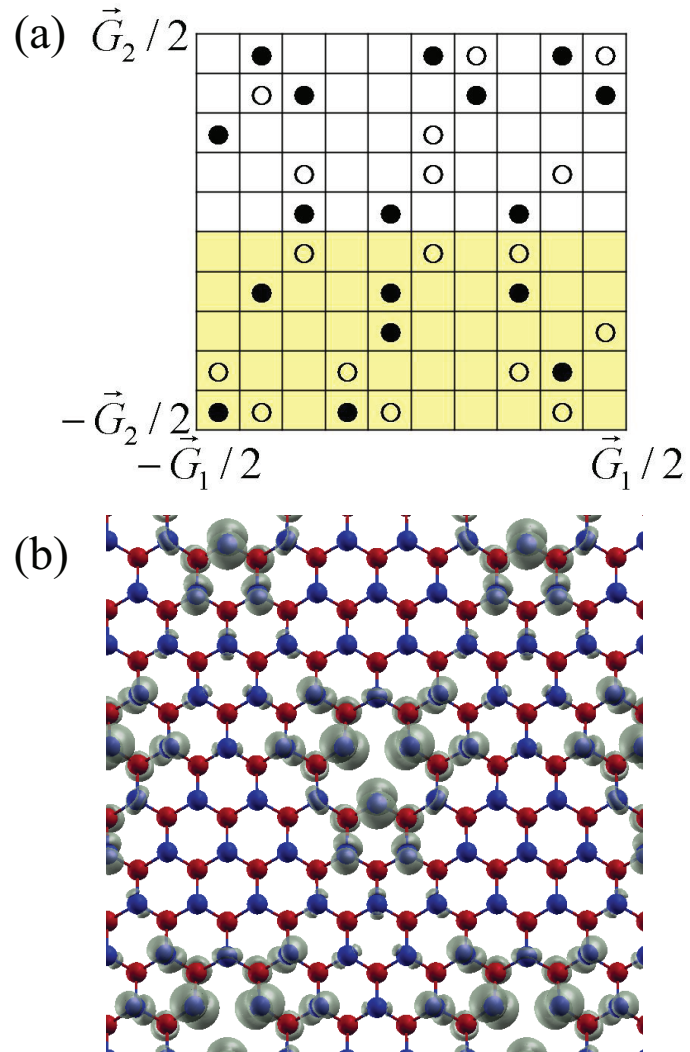


Figure 3.11: The n-field configuration and wavefunction of the upper TNNBs. (a) The n-field configuration of the upper TNNBs showing the nontrivial band topology. (b) The absolute square of the wavefunction of the upper TNNBs at the Γ point.

reflecting the figure with respect to the $k = 0$ axis.)

The band topology of the system can be changed if the Fermi level is shifted by charge doping, which changes the number of occupied bands. Because the additional charges can affect the forces between atoms and in turn change the electronic band dispersion, we perform the calculations of the charged configurations (with compensating background charges) including the atomic relaxation calculations. When two electrons are doped in the Sn-Te bilayer with Sn vacancies in 5×5 periodicity, the Fermi level lies above the upper TNNBs and the system becomes a NI, which can be seen by the absence of the edge states near the Fermi level (Fig. 3.13). Thus, the topological change by charge doping is a way to manipulate the topological edge states; we can switch on and off the topological edge states by charge doping. Also, if we dope two holes, the Fermi level is set below the lower TNNBs and the system becomes a NI (Fig. 3.14).

We can devise an another type of defect superstructure to have a topological phase: Te vacancies in 5×5 periodicity with 3 neighboring Sn atoms replaced by Sb and a hole doping. The atomic structure is presented in Fig. 3.15. The replacement of the 3 Sn atoms by Sb atoms is devised by considering the nominal charge count compared with the previous Sn vacancy case while preserving the local three-fold symmetry. The band structure shows two TNNBs in this case and the Fermi level lies in the upper TNNBs, i.e., the system is metallic in its natural electron filling. To have a TI phase, the system needs to be doped by 1 hole to set the Fermi level between the two TNNBs. Indeed, if we perform the charged cell calculation with 1 hole per cell, we have

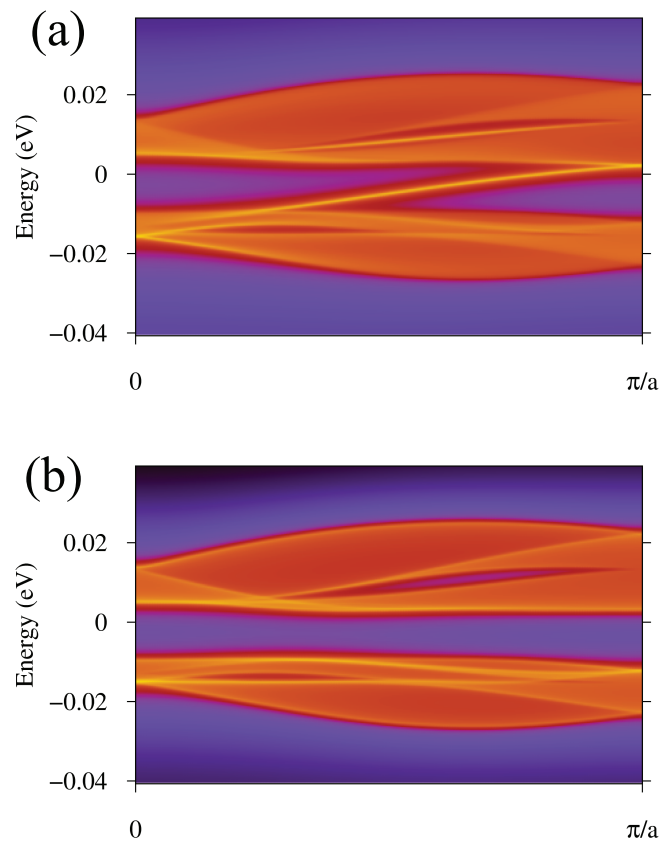


Figure 3.12: EMLDOS for the Sn-Te bilayer with the Sn vacancy superstructure. (a) EMLDOS of the edge layer. (b) EMLDOS of the bulk layer. The topological gapless edge states appear in (a).

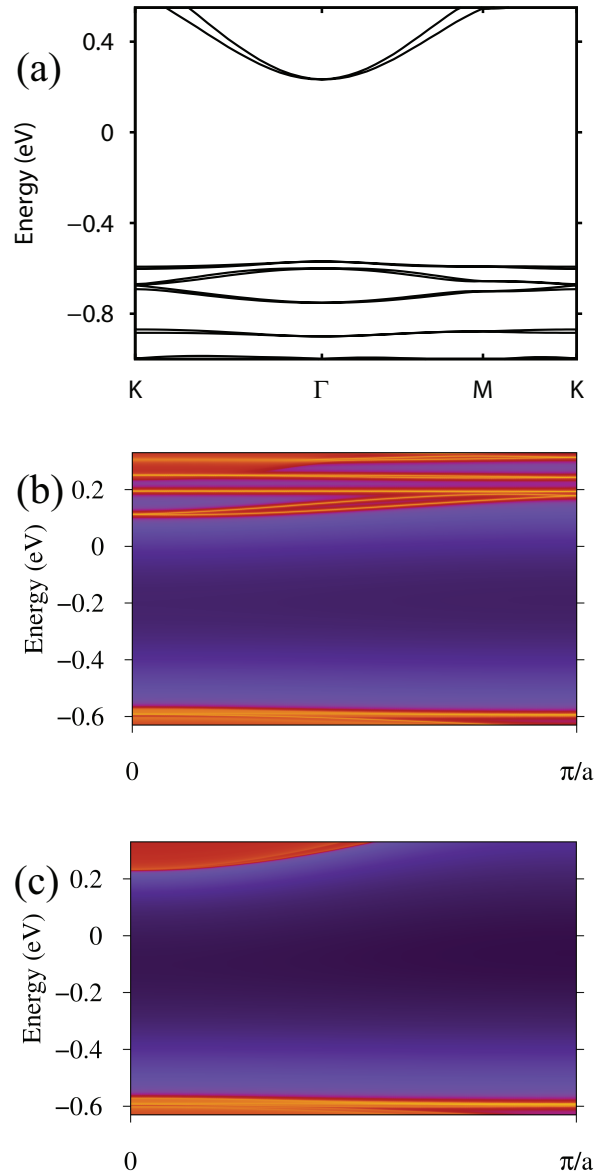


Figure 3.13: Band structure and EMLDOS for the Sn-Te bilayer with the Sn vacancy superstructure with two electrons doped. (a) The band structure, (b) EMLDOS of the edge layer, and (c) EMLDOS of the bulk layer are depicted for the two electron doping case.

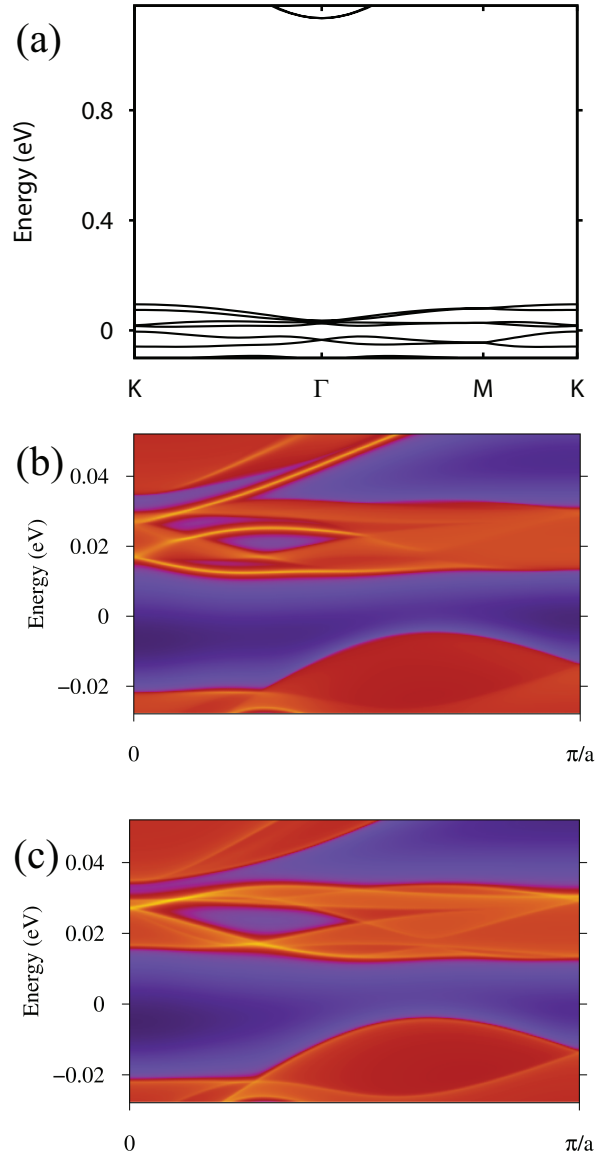


Figure 3.14: Band structure and EMLDOS for the Sn-Te bilayer with the Sn vacancy superstructure with two holes doped. (a) The band structure, (b) EMLDOS of the edge layer, and (c) EMLDOS of the bulk layer are depicted for the two hole doping case.

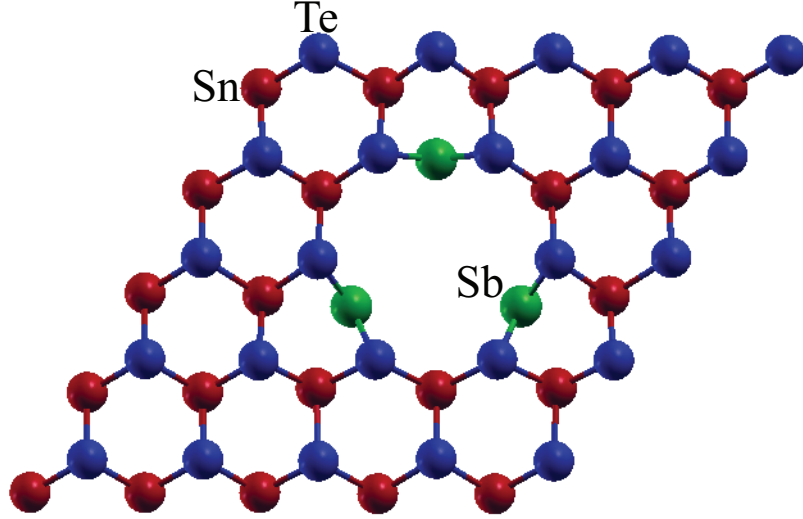


Figure 3.15: Atomic structure of the Sn-Te bilayer with the Te vacancy, 3 Sb substitutions and a hole doping in 5×5 periodicity.

a TI phase (Fig. 3.16), where $\nu = 1$ is obtained according to our \mathbb{Z}_2 invariant calculations. The size of the energy gap is estimated to be $\simeq 8$ meV. Accordingly, the edge state configuration shows the topologically nontrivial behavior (Fig. 3.17). The topological phase change by charge doping is also possible. If we dope the system by an electron instead of a hole, the Fermi level moves above the upper TNNBs. Then, the system becomes a NI as illustrated by the edge state dispersion in Fig. 3.18.

We assumed the formation of defect superstructures throughout this study. This assumption might be affected by the presence of disorders in the positions of defects in real systems. Because disorders may affect the topological character [28], more general theory is needed to include the disorder effects. Additional cap layers and substrates might be helpful to fix the defect struc-

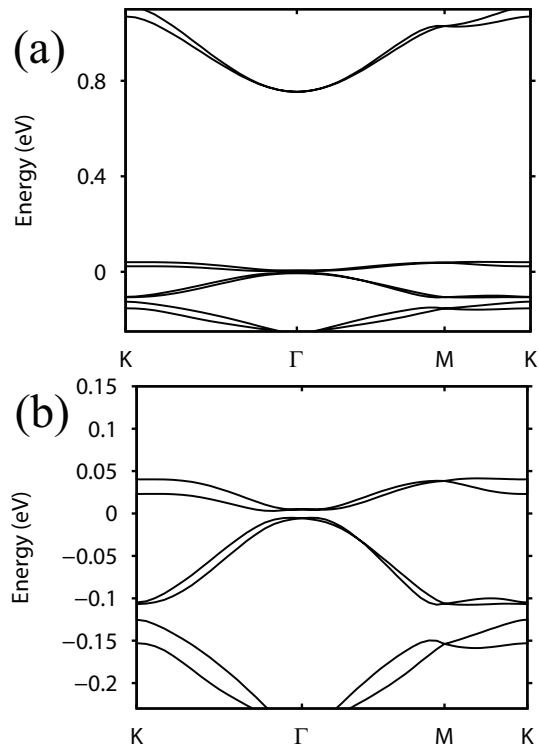


Figure 3.16: Electronic structure of the Sn-Te bilayer with the Te vacancy, the Sb substitution and a hole doping in 5×5 periodicity. (a) Band structure of the system. (b) Band structure near the Fermi energy.

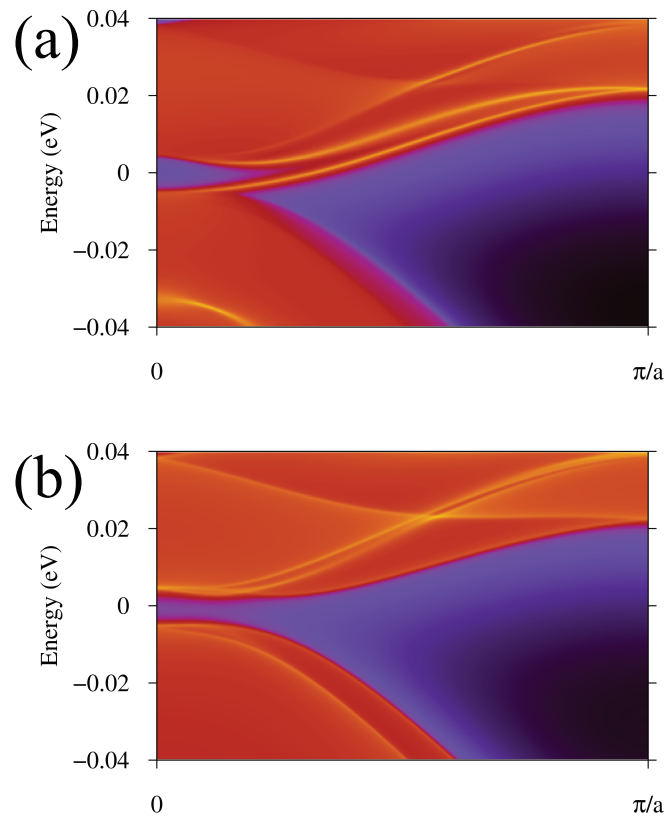


Figure 3.17: EMLDOS for the Sn-Te bilayer with the Te vacancy, the Sb substitution and a hole doping in 5×5 periodicity. (a) EMLDOS of the edge layer. (b) EMLDOS of the bulk layer. The topological gapless edge states are present in (a).

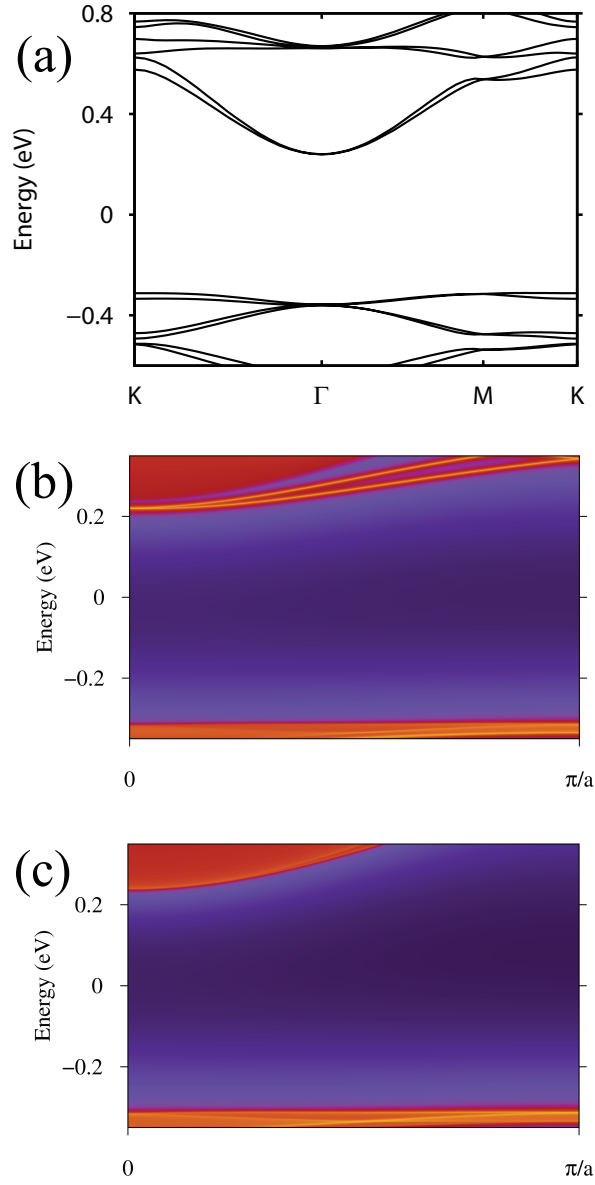


Figure 3.18: Band structure and EMLDOS for the Sn-Te bilayer with the Te vacancy, the Sb substitution and an electron doping in 5×5 periodicity. (a) The band structure, (b) EMLDOS of the edge layer, and (c) EMLDOS of the bulk layer are depicted for the one electron doping case.

tures as desired while keeping the essential topological spin-orbit splitting near the Fermi energy.

3.2.3 Conclusions

In conclusion, we investigated the topology of the defect-induced bands and showed that the Sn-Te bilayer can be transformed from a NI to a TI by introducing the periodic array of defects. We predicted the formation of TNNBs near the Fermi energy originating from the topologically nontrivial spin-orbit splitting of the defect-induced bands. We devised two examples: the Sn-Te bilayer with the Sn vacancy 5×5 periodicity and the Sn-Te bilayer with the Te vacancy, 3 Sb substitutions and a hole doping in 5×5 periodicity. Furthermore, it was shown that the systems undergo phase transitions between a TI and a NI phases by the charge doping due to the narrow band width of the topological defect-induced bands. Our results would be important to realize a 2D TI phase and provide a convenient mechanism to control the topologically robust edge conducting states by charge doping.

3.2.4 Methods

We performed density functional theory calculations as implemented in Quantum Espresso package [45]. We used PBE (Perdew-Burke-Ernzerhof) exchange-correlation functional [6]. Fully relativistic pseudopotentials were used to include the SOC effects. Scalar relativistic pseudopotentials were also used to check the electronic band structure without the SOC. The energy cutoff of the planewave basis set was 35 Ry. The experimental lattice constant was

used [57]. The internal atomic coordinates were relaxed until the force components became less than 0.026 eV/\AA . The calculation of the \mathbb{Z}_2 invariant was performed by employing the lattice computation method [33, 34]. The construction of Wannier functions was done by using Wannier90 package [47]. We calculated the edge and bulk layer EMLDOS using the Green function method [35, 36].

Chapter 4

Rashba splittings

4.1 Polarization-dependent angular momentum textures of $S = 1/2$ and $J = 1/2$ Rashba bands in ferroelectric hybrid metal halide perovskites

4.1.1 Introduction

The Rashba effect is spin degeneracy lifting that results from the broken inversion symmetry and the SOC [58], which has been investigated in 2D surfaces, interfaces, quantum wells, and 3D materials [59, 60, 61, 62, 63]. (When both the time reversal symmetry and inversion symmetry are present, the spin degeneracy is kept in the entire BZ: $E_{\vec{k}\uparrow} = E_{-\vec{k}\downarrow} = E_{\vec{k}\downarrow}$.) Because the formation of the 2D surface breaks the inversion symmetry of 3D bulk Hamiltonian, the surface states, for example, in Au (111) surfaces show the Rashba band splitting [59]. Also, recent studies show that larger size of the Rashba split-

ting can be obtained by surface alloying [60] and in quantum wells [62]. The Hamiltonian for the Rashba splitting can be written as

$$\mathcal{H}_R = \alpha_R(\hat{e} \times \vec{k}) \cdot \vec{\sigma}, \quad (4.1)$$

in which α_R is the Rashba coefficient, \hat{e} is a unit vector, \vec{k} is the crystal momentum, and the components of $\vec{\sigma}$ are the Pauli matrices. The size of the Rashba splitting is characterized by α_R and the Rashba split bands have helical spin texture whose direction is determined by the unit vector \hat{e} .

Although the size of the Rashba splitting has been of principal concern, the controllability in the direction of the inversion symmetry breaking (ISB) field (the unit vector \hat{e} in Eq. 4.1) has not been studied seriously. In 2D surfaces or interfaces, the direction of the ISB field is mainly determined by the termination of the material. In 3D Rashba materials such as BiTeI, the direction of the ISB polarization is fixed by the compositional ISB of the Te and I layers [63]. Here, we consider a mechanism to control the direction of the ISB polarization using external electric fields by employing ferroelectric Rashba materials. In a ferroelectric system, the direction of the polarization can be reversed by external fields. Because the helical directions of the spin textures in the Rashba bands are coupled to the direction of the ISB polarization, the spin texture directions can be controlled by external fields. Compared with the previous reports of the gate-controlled Rashba SOC in the 2D heterostructure and quantum well experiments [64, 65], the ferroelectric Rashba material can provide more effective way to manipulate the ISB field. Recently, there was a

theoretical study of GeTe as a candidate for the ferroelectric Rashba material. However, due to the sizable conductivity in bulk GeTe, the direct measurement of the electric polarization and the ferroelectric switching is still missing [66, 67].

We consider the organic-inorganic hybrid metal halide perovskites as possible candidates for ferroelectric Rashba materials. Specifically, the materials with a chemical formula AMX_3 will be considered, where A is an organic molecule (typically, CH_3NH_3 , i.e., methylammonium (MA)), M is Pb or Sn, and X is I or Br. In contrast to GeTe, clear ferroelectric response is measured experimentally in the hybrid metal halide perovskites [69]. Also, as will be shown, the Rashba bands of the hybrid halide perovskites appear at a single k -point in BZ with almost isotropic dispersions whereas GeTe has multiple band edges and hexagonal warping. Therefore, the hybrid halide perovskites are ideal 3D Rashba systems with good material quality.

Another intriguing property of the halide perovskites is that two contrasting ($S = 1/2$ and $J = 1/2$) Rashba bands appear simultaneously in the electronic structure (Fig. 4.1). Due to the original band character of the halide perovskites, there appear $S = 1/2$ Rashba bands at the valence band maximum (VBM) and $J = 1/2$ Rashba bands at the conduction band minimum (CBM). In terms of the Rashba Hamiltonian (Eq. 4.1), the two different types of Rashba bands correspond to the different splitting subspaces described by the Pauli matrices $\vec{\sigma}$. The crystal field and SOC can affect the character of the bands. If the crystal field is dominant, the splitting space will be the spin space. If the SOC dominates, the splitting space will be the total angular

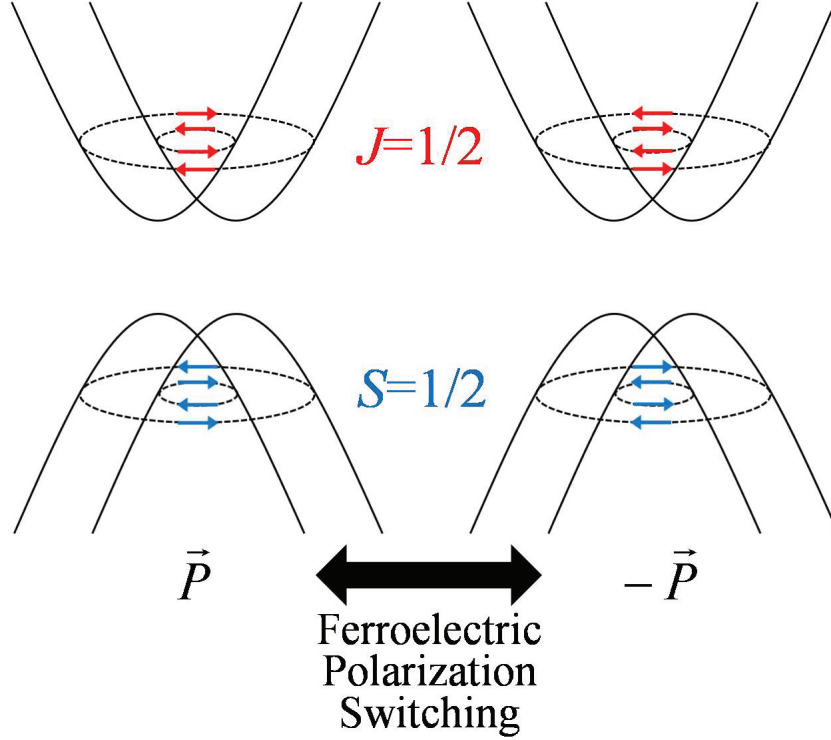


Figure 4.1: Schematic illustration of the switchable $S = 1/2$ and $J = 1/2$ Rashba effect via ferroelectric switching.

momentum space.

In this section, we report a theoretical investigation of the electronic structures of the organic-inorganic hybrid metal halide perovskites [70]. Using minimal tight-binding (TB) model Hamiltonian, we show that the materials have $S = 1/2$ and $J = 1/2$ Rashba bands that are coupled to the ferroelectric polarization. With the recent experimental evidence of the ferroelectric property [69], the hybrid halide perovskites are promising candidates for the ferroelectric Rashba system. The origin of the splitting in the $S = 1/2$ Rashba bands is ascribed to the interband coupling between the s and p bands, whereas

that in the $J = 1/2$ Rashba bands is attributed to the intraband coupling within the $J = 1/2$ manifold as well as the s - p interband coupling. We examine the electronic structure of real materials (β -MAPbI₃ and β -MASnI₃) by first-principles calculations based on density functional theory. The representative example is chosen to be MAPbI₃ and it is found that the material has the characteristic features of the TB model and the sizable Rashba coefficient α_R . Also, we discuss a different type of controllability. We show that the relative helicity changes between the two Rashba bands are possible by adjusting the positions of the lateral X atoms.

4.1.2 Results and Discussion

We first introduce the basic information on the electronic structure of the metal halide perovskites. In AMX₃ halide perovskites, the nominal oxidation states of A, M, and X are +1, +2, and -1, respectively. Here, s and p states of M, and p states of X are important for the physics near the Fermi energy (A is chemically inert). In the cubic phase of the halide perovskites [71] (for example, CsPbI₃), without SOC, the VBM consists of a single $L = 0$ band that comes from the s states of M and p states of X, and the CBM consists of triply degenerate $L = 1$ bands that come from the p states of M due to the cubic crystal field. Upon including the effect of the SOC, the CBM states split into $J = 1/2$ and $J = 3/2$ states whereas the VBM states are not affected, which results in $J = 1/2$ bands at the CBM and $S = 1/2$ bands at the VBM.

We construct a minimal TB model based on the above electronic structure information. We choose s and p states in a cubic lattices as the basis and

consider the Hamiltonian

$$H = H_{\text{hop}} + H_{\text{SOC}} + H_{\text{ISB}}, \quad (4.2)$$

where H_{hop} is the hopping term, H_{SOC} is the SOC term and H_{ISB} describes the effect of the polar distortion that breaks the inversion symmetry. If we omit H_{ISB} , the Hamiltonian describes the cubic phase of the halides [71]. In H_{hop} term, we consider the nearest-neighbor hopping in the 3D cubic lattice with s and p states at the center of the cubic cell. The hopping matrix is

$$H_{\text{hop}, \vec{R}} = \begin{pmatrix} t_{ss\sigma} & ut_{sp\sigma} & vt_{sp\sigma} & wt_{sp\sigma} \\ -ut_{sp\sigma} & u^2t_{pp\sigma} + (1-u^2)t_{pp\pi} & uv(t_{pp\sigma} - t_{pp\pi}) & uw(t_{pp\sigma} - t_{pp\pi}) \\ -vt_{sp\sigma} & uv(t_{pp\sigma} - t_{pp\pi}) & v^2t_{pp\sigma} + (1-v^2)t_{pp\pi} & vw(t_{pp\sigma} - t_{pp\pi}) \\ -wt_{sp\sigma} & uw(t_{pp\sigma} - t_{pp\pi}) & vw(t_{pp\sigma} - t_{pp\pi}) & w^2t_{pp\sigma} + (1-w^2)t_{pp\pi} \end{pmatrix},$$

with the basis $\{|s\rangle, |p_x\rangle, |p_y\rangle, |p_z\rangle\}$. \vec{R} is the vector connecting the neighboring basis orbitals with $\hat{R} = (u, v, w)$. In the case of the H_{SOC} , we consider the atomic SOC of the M atom in the s and p manifolds

$$H_{\text{SOC}} = \frac{\lambda}{2} \begin{pmatrix} 0 & 0 & 0 & 0 & 0 & 0 & 0 & 0 \\ 0 & 0 & -i & 0 & 0 & 0 & 0 & 1 \\ 0 & i & 0 & 0 & 0 & 0 & 0 & -i \\ 0 & 0 & 0 & 0 & 0 & -1 & i & 0 \\ 0 & 0 & 0 & 0 & 0 & 0 & 0 & 0 \\ 0 & 0 & 0 & -1 & 0 & 0 & i & 0 \\ 0 & 0 & 0 & -i & 0 & -i & 0 & 0 \\ 0 & 1 & i & 0 & 0 & 0 & 0 & 0 \end{pmatrix},$$

with the basis $\{|s \uparrow\rangle, |p_x \uparrow\rangle, |p_y \uparrow\rangle, |p_z \uparrow\rangle, |s \downarrow\rangle, |p_x \downarrow\rangle, |p_y \downarrow\rangle, |p_z \downarrow\rangle\}$. In the

H_{ISB} term, the additional hopping elements that arise from the ISB field \vec{E}_{ISB} is considered. If the ISB field is parallel to the z direction, the additional orbital mixings are

$$\gamma_{spz} = \langle s | (\vec{E}_{\text{ISB}})_z z | p_z, \hat{e}_x \rangle = \langle s | (\vec{E}_{\text{ISB}})_z z | p_z, \hat{e}_y \rangle, \quad (4.3)$$

and

$$\gamma_{ppz} = \langle p_x | (\vec{E}_{\text{ISB}})_z z | p_z, \hat{e}_x \rangle = \langle p_y | (\vec{E}_{\text{ISB}})_z z | p_z, \hat{e}_y \rangle, \quad (4.4)$$

where \hat{e}_x and \hat{e}_y denotes the vector connecting the neighboring sites in the x and y directions, respectively. Here, the lattice constant is set to 1. Similarly, we can define γ_{spx} , γ_{spy} , γ_{ppx} , and γ_{ppy} as

$$\begin{aligned} \gamma_{spx} &= \langle s | (\vec{E}_{\text{ISB}})_x x | p_x, \hat{e}_y \rangle = \langle s | (\vec{E}_{\text{ISB}})_x x | p_x, \hat{e}_z \rangle, \\ \gamma_{spy} &= \langle s | (\vec{E}_{\text{ISB}})_y y | p_y, \hat{e}_z \rangle = \langle s | (\vec{E}_{\text{ISB}})_y y | p_y, \hat{e}_x \rangle, \\ \gamma_{ppx} &= \langle p_y | (\vec{E}_{\text{ISB}})_x x | p_x, \hat{e}_y \rangle = \langle p_z | (\vec{E}_{\text{ISB}})_x x | p_x, \hat{e}_z \rangle, \\ \gamma_{ppy} &= \langle p_z | (\vec{E}_{\text{ISB}})_y y | p_y, \hat{e}_z \rangle = \langle p_x | (\vec{E}_{\text{ISB}})_y y | p_y, \hat{e}_x \rangle. \end{aligned} \quad (4.5)$$

For the field with a general direction, defining $\vec{\gamma}_{sp} = (\gamma_{spx}, \gamma_{spy}, \gamma_{spz})$ and $\vec{\gamma}_{pp} = (\gamma_{ppx}, \gamma_{ppy}, \gamma_{ppz})$, the orbital mixings from the ISB field become

$$H_{\text{ISB}, \vec{R}} = \begin{pmatrix} 0 & \vec{\gamma}_{sp} \cdot (\hat{x} - u\hat{R}) & \vec{\gamma}_{sp} \cdot (\hat{y} - v\hat{R}) & \vec{\gamma}_{sp} \cdot (\hat{z} - w\hat{R}) \\ \vec{\gamma}_{sp} \cdot (\hat{x} - u\hat{R}) & 0 & \vec{\gamma}_{pp} \cdot (\hat{z} \times \hat{R}) & -\vec{\gamma}_{pp} \cdot (\hat{y} \times \hat{R}) \\ \vec{\gamma}_{sp} \cdot (\hat{y} - v\hat{R}) & -\vec{\gamma}_{pp} \cdot (\hat{z} \times \hat{R}) & 0 & \vec{\gamma}_{pp} \cdot (\hat{x} \times \hat{R}) \\ \vec{\gamma}_{sp} \cdot (\hat{z} - w\hat{R}) & \vec{\gamma}_{pp} \cdot (\hat{y} \times \hat{R}) & -\vec{\gamma}_{pp} \cdot (\hat{x} \times \hat{R}) & 0 \end{pmatrix},$$

where \hat{x} , \hat{y} , and \hat{z} are the unit vectors along the x , y , and z direction, respectively. Combining the terms, the total Hamiltonian $H(\vec{k})$ becomes

$$H(\vec{k}) = \begin{pmatrix} \epsilon_s + T_{ss} & A_{spx} & A_{spy} & A_{spz} & 0 & 0 & 0 & 0 \\ A_{spx}^* & \epsilon_p + T_{ppx} & -\frac{\lambda}{2}i - \Gamma_{ppxy} & \Gamma_{ppzx} & 0 & 0 & 0 & \frac{\lambda}{2} \\ A_{spy}^* & \frac{\lambda}{2}i + \Gamma_{ppxy} & \epsilon_p + T_{ppy} & -\Gamma_{ppyz} & 0 & 0 & 0 & -\frac{\lambda}{2}i \\ A_{spz}^* & -\Gamma_{ppzx} & \Gamma_{ppyz} & \epsilon_p + T_{ppz} & 0 & -\frac{\lambda}{2} & \frac{\lambda}{2}i & 0 \\ 0 & 0 & 0 & 0 & \epsilon_s + T_{ss} & A_{spx} & A_{spy} & A_{spz} \\ 0 & 0 & 0 & -\frac{\lambda}{2} & A_{spx}^* & \epsilon_p + T_{ppx} & \frac{\lambda}{2}i - \Gamma_{ppxy} & \Gamma_{ppzx} \\ 0 & 0 & 0 & -\frac{\lambda}{2}i & A_{spy}^* & -\frac{\lambda}{2}i + \Gamma_{ppxy} & \epsilon_p + T_{ppy} & -\Gamma_{ppyz} \\ 0 & \frac{\lambda}{2} & \frac{\lambda}{2}i & 0 & A_{spz}^* & -\Gamma_{ppzx} & \Gamma_{ppyz} & \epsilon_p + T_{ppz} \end{pmatrix},$$

with the basis $\{|s \uparrow\rangle, |p_x \uparrow\rangle, |p_y \uparrow\rangle, |p_z \uparrow\rangle, |s \downarrow\rangle, |p_x \downarrow\rangle, |p_y \downarrow\rangle, |p_z \downarrow\rangle\}$. Here,

$$\begin{aligned} T_{ss} &= 2t_{ss\sigma}(\cos k_x + \cos k_y + \cos k_z), \\ T_{ppx} &= 2t_{pp\sigma} \cos k_x + 2t_{pp\pi}(\cos k_y + \cos k_z), \\ A_{spx} &= 2it_{sp\sigma} \sin k_x + 2\gamma_{spx}(\cos k_y + \cos k_z), \\ \Gamma_{ppxy} &= 2i\gamma_{ppx} \sin k_y - 2i\gamma_{ppy} \sin k_x. \end{aligned}$$

If we perform a unitary transformation to the total angular momentum J basis,

the Hamiltonian becomes

$$H(\vec{k}) = \begin{pmatrix} \epsilon_s + T_{ss} & 0 & \frac{-iQ_z - \Gamma_{1z}}{\sqrt{3}} & \frac{-iQ^- - \Gamma_1^-}{\sqrt{3}} & \frac{-iQ^+ - \Gamma_1^+}{\sqrt{2}} & \frac{iQ_z + \Gamma_{1z}}{\sqrt{3}/\sqrt{2}} & \frac{iQ^- + \Gamma_1^-}{\sqrt{6}} & 0 \\ 0 & \epsilon_s + T_{ss} & \frac{-iQ^+ - \Gamma_1^+}{\sqrt{3}} & \frac{iQ_z + \Gamma_{1z}}{\sqrt{3}} & 0 & \frac{-iQ^- - \Gamma_1^-}{\sqrt{6}} & \frac{iQ_z + \Gamma_{1z}}{\sqrt{3}/\sqrt{2}} & \frac{iQ^- + \Gamma_1^-}{\sqrt{2}} \\ \frac{iQ_z - \Gamma_{1z}}{\sqrt{3}} & \frac{iQ^- - \Gamma_1^-}{\sqrt{3}} & \epsilon_{p1} + \frac{2\Gamma_{2xy}}{3} & \frac{2\Gamma_2^-}{3} & -\frac{\Gamma_2^+}{\sqrt{6}} & \frac{P'_z + \Gamma_{2xy}}{3\sqrt{2} + 3/\sqrt{2}} & \frac{\sqrt{2}\Gamma_2^-}{6} & -\frac{P_x - P_y}{\sqrt{6}} \\ \frac{iQ^+ - \Gamma_1^+}{\sqrt{3}} & \frac{-iQ_z + \Gamma_{1z}}{\sqrt{3}} & \frac{2\Gamma_2^+}{3} & \epsilon_{p1} - \frac{2\Gamma_{2xy}}{3} & \frac{P_x - P_y}{\sqrt{6}} & -\frac{\sqrt{2}\Gamma_2^+}{6} & \frac{-P'_z + \Gamma_{2xy}}{3\sqrt{2} + 3/\sqrt{2}} & \frac{\Gamma_2^-}{\sqrt{6}} \\ \frac{iQ^- - \Gamma_1^-}{\sqrt{2}} & 0 & -\frac{\Gamma_2^-}{\sqrt{6}} & \frac{P_x - P_y}{\sqrt{6}} & \epsilon_{p3} + \Gamma_{2xy} & \frac{\Gamma_2^-}{\sqrt{3}} & -\frac{P_x - P_y}{2\sqrt{3}} & 0 \\ \frac{-iQ_z + \Gamma_{1z}}{\sqrt{3}/\sqrt{2}} & \frac{iQ^- - \Gamma_1^-}{\sqrt{6}} & \frac{P'_z + \Gamma_{2xy}}{3\sqrt{2} + 3/\sqrt{2}} & -\frac{\sqrt{2}\Gamma_2^-}{6} & \frac{\Gamma_2^+}{\sqrt{3}} & \epsilon_{p2} + \frac{\Gamma_{2xy}}{3} & \frac{2\Gamma_2^-}{3} & -\frac{P_x - P_y}{2\sqrt{3}} \\ \frac{-iQ^+ + \Gamma_1^+}{\sqrt{6}} & \frac{-iQ_z + \Gamma_{1z}}{\sqrt{3}/\sqrt{2}} & \frac{\sqrt{2}\Gamma_2^+}{6} & \frac{-P'_z + \Gamma_{2xy}}{3\sqrt{2} + 3/\sqrt{2}} & -\frac{P_x - P_y}{2\sqrt{3}} & \frac{2\Gamma_2^+}{3} & \epsilon_{p2} - \frac{\Gamma_{2xy}}{3} & \frac{\Gamma_2^-}{\sqrt{3}} \\ 0 & \frac{-iQ^+ + \Gamma_1^+}{\sqrt{2}} & -\frac{P_x - P_y}{\sqrt{6}} & \frac{\Gamma_2^+}{\sqrt{6}} & 0 & -\frac{P_x - P_y}{2\sqrt{3}} & \frac{\Gamma_2^+}{\sqrt{3}} & \epsilon_{p3} - \Gamma_{2xy} \end{pmatrix},$$

with the basis $\{|s \uparrow\rangle, |s \downarrow\rangle, |j = \frac{1}{2} j_z = \frac{1}{2}\rangle, |j = \frac{1}{2} j_z = -\frac{1}{2}\rangle, |j = \frac{3}{2} j_z = \frac{3}{2}\rangle, |j = \frac{3}{2} j_z = \frac{1}{2}\rangle, |j = \frac{3}{2} j_z = -\frac{1}{2}\rangle, |j = \frac{3}{2} j_z = -\frac{3}{2}\rangle\}$. Here,

$$T_{ss} = 2t_{ss\sigma}(\cos k_x + \cos k_y + \cos k_z),$$

$$Q_x = 2t_{sp\sigma} \sin k_x,$$

$$Q^\pm = Q_x \pm iQ_y,$$

$$\Gamma_{1x} = 2\gamma_{spx}(\cos k_y + \cos k_z).$$

$$\Gamma_1^\pm = \Gamma_{1x} \pm i\Gamma_{1y},$$

$$\Gamma_{2xy} = 2\gamma_{ppx} \sin k_y - 2\gamma_{ppy} \sin k_x.$$

$$\Gamma_2^\pm = \Gamma_{2yz} \pm i\Gamma_{2zx},$$

and

$$\begin{aligned}
\epsilon_{p1} &= \epsilon_p + \frac{P_x + P_y + P_z}{3} - \lambda, \\
\epsilon_{p2} &= \epsilon_p + \frac{P_x + P_y + 4P_z}{6} + \frac{\lambda}{2}, \\
\epsilon_{p3} &= \epsilon_p + \frac{P_x + P_y}{2} + \frac{\lambda}{2}, \\
P_x &= 2t_{pp\sigma} \cos k_x + 2t_{pp\pi}(\cos k_y + \cos k_z), \\
P'_z &= P_x + P_y - 2P_z.
\end{aligned}$$

By numerically diagonalizing the TB Hamiltonian, we obtain the band structure (Fig. 4.2(a)). The VBM and CBM are located at the A point of the BZ (tetragonal index), and the $S = 1/2$ states appear at the VBM and $J = 1/2$ states, at the CBM. If the ISB field is introduced in the z direction, the band edges states at the VBM and CBM show the Rashba band splittings (Fig. 4.2(b)). To understand the band splittings, we derive the effective Hamiltonian near the Fermi energy. The effective Hamiltonian can be obtained by using

$$H_{eff} = PHP + PHQ \frac{1}{\epsilon - QHQ} QHP, \quad (4.6)$$

in which P is the projection operator onto the relevant subspace (s states for VBM and $J = 1/2$ states for CBM) and $Q = 1 - P$. For VBM, the resultant effective Hamiltonian is given by

$$H_{eff,VBM} = h_v(\vec{k})I + \frac{-8\lambda t_{sp\sigma}}{(\Delta_{sp} + \lambda)(\Delta_{sp} - \frac{\lambda}{2})} (\vec{\gamma}_{sp} \times \vec{k}) \cdot \vec{\tau}_{S=1/2}, \quad (4.7)$$

where

$$\begin{aligned}
h_v(\vec{k}) &= \epsilon_s - 6t_{ss\sigma} + \frac{16(\Delta_{sp} + \frac{\lambda}{2})}{(\Delta_{sp} + \lambda)(\Delta_{sp} - \frac{\lambda}{2})} \gamma_{sp}^2 \\
&\quad + \left\{ t_{ss\sigma} + \frac{4(\Delta_{sp} + \frac{\lambda}{2})}{(\Delta_{sp} + \lambda)(\Delta_{sp} - \frac{\lambda}{2})} t_{sp\sigma}^2 \right\} k^2 \\
&\quad - \frac{8(\Delta_{sp} + \frac{\lambda}{2})}{(\Delta_{sp} + \lambda)(\Delta_{sp} - \frac{\lambda}{2})} \{ (\gamma_{spy}^2 + \gamma_{spz}^2) k_x^2 + (\gamma_{spz}^2 + \gamma_{spx}^2) k_y^2 + (\gamma_{spx}^2 + \gamma_{spy}^2) k_z^2 \}, \\
\Delta_{sp} &= \epsilon_s - 6t_{ss\sigma} - \epsilon_p + 2t_{pp\sigma} + 4t_{pp\pi}, \\
\text{cf. } &\frac{-8\lambda t_{sp\sigma}}{(\Delta_{sp} + \lambda)(\Delta_{sp} - \frac{\lambda}{2})} = \frac{\frac{16}{3} t_{sp\sigma}}{\Delta_{sp} + \lambda} - \frac{\frac{16}{3} t_{sp\sigma}}{\Delta_{sp} - \frac{\lambda}{2}}.
\end{aligned}$$

In the case of CBM, we obtain

$$\begin{aligned}
H_{eff,CBM} &= h_c(\vec{k})I + \frac{-\frac{16}{3} t_{sp\sigma}}{\Delta_{ps} - \lambda} (\vec{\gamma}_{sp} \times \vec{k}) \cdot \vec{\tau}_{J=1/2} - \frac{4}{3} (\vec{\gamma}_{pp} \times \vec{k}) \cdot \vec{\tau}_{J=1/2} \\
&= h_c(\vec{k})I + (\vec{\gamma}' \times \vec{k}) \cdot \vec{\tau}_{J=1/2}, \tag{4.8}
\end{aligned}$$

where

$$\begin{aligned}
h_c(\vec{k}) &= \epsilon_p - 2t_{pp\sigma} - 4t_{pp\pi} - \lambda + \left(\frac{t_{pp\sigma}}{3} + \frac{2t_{pp\pi}}{3} \right) k^2 \\
&\quad + \frac{4t_{sp\sigma}^2 k^2 + 16\gamma_{sp}^2 - 8(\gamma_{spy}^2 + \gamma_{spz}^2) k_x^2 - 8(\gamma_{spz}^2 + \gamma_{spx}^2) k_y^2 - 8(\gamma_{spx}^2 + \gamma_{spy}^2) k_z^2}{3(\Delta_{ps} - \lambda)} \\
&\quad - \frac{16}{27\lambda} \{ (\gamma_{ppy}^2 + \gamma_{ppz}^2) k_x^2 + (\gamma_{ppz}^2 + \gamma_{ppx}^2) k_y^2 + (\gamma_{ppx}^2 + \gamma_{ppy}^2) k_z^2 \\
&\quad \quad - 2\gamma_{ppx}\gamma_{ppy}k_xk_y - 2\gamma_{ppy}\gamma_{ppz}k_yk_z - 2\gamma_{ppz}\gamma_{ppx}k_zk_x \}, \\
\Delta_{ps} &= \epsilon_p - 2t_{pp\sigma} - 4t_{pp\pi} - \epsilon_s + 6t_{ss\sigma}, \\
\vec{\gamma}' &= \frac{-\frac{16}{3} t_{sp\sigma}}{\Delta_{ps} - \lambda} \vec{\gamma}_{sp} - \frac{4}{3} \vec{\gamma}_{pp}.
\end{aligned}$$

Here, λ is the SOC parameter, t are the hopping parameters, \vec{k} is the crys-

tal momentum. The functions $h_v(\vec{k})$ and $h_c(\vec{k})$ describe the quadratic band dispersion. Also, $\vec{\tau}_{S=1/2}$ and $\vec{\tau}_{J=1/2}$ describe the $S = 1/2$ and $J = 1/2$ degrees of freedom, respectively. The effective Hamiltonians have splitting terms whose form is the Bychkov-Rashba Hamiltonian [58] coupled to the ferroelectric polarization. The Rashba-split bands have helical angular momentum textures (Fig. 4.3). We assign the helical direction according to the direction of the spin (orbital) angular momentum in VBM (CBM) because the principal contributions come from the spin (orbital) part. If the direction of the polarization is reversed by ferroelectric switching, the directions of $\vec{\gamma}_{sp}$ and $\vec{\gamma}_{pp}$ are reversed, and the helical angular momentum textures are also reversed accordingly. Thus, the helical direction of the angular momentum texture in the Rashba bands are controlled by ferroelectric switching. It is to be noted that the helicity reversal is not dependent on the specific form of the effective Hamiltonian. The configuration with the opposite polarization is obtained by the spatial inversion operation. Under the inversion operation, the crystal momentum \vec{k} becomes $-\vec{k}$ whereas the angular momentum is not changed because the angular momentum is an axial vector. We consider the wavefunctions $|\psi_{\vec{k}, \vec{P}}\rangle$ in the polarization \vec{P} configuration and $|\phi_{\vec{k}', -\vec{P}}\rangle$ in the polarization $-\vec{P}$ configuration. Then, for the expectation value of an angular momentum

operator $\hat{\mathbf{J}}$, we have

$$\begin{aligned}
\mathbf{J}_{\vec{k}, -\vec{P}} &= \langle \phi_{\vec{k}}, -\vec{P} | \hat{\mathbf{J}} | \phi_{\vec{k}}, -\vec{P} \rangle \\
&= \langle \phi_{-\vec{k}}, -\vec{P} | T^{-1} \hat{\mathbf{J}} T | \phi_{-\vec{k}}, -\vec{P} \rangle \\
&= \langle \psi_{\vec{k}}, \vec{P} | I^{-1} T^{-1} \hat{\mathbf{J}} T I | \psi_{\vec{k}}, \vec{P} \rangle \\
&= \langle \psi_{\vec{k}}, \vec{P} | I^{-1} (-\hat{\mathbf{J}}) I | \psi_{\vec{k}}, \vec{P} \rangle \\
&= \langle \psi_{\vec{k}}, \vec{P} | -\hat{\mathbf{J}} | \psi_{\vec{k}}, \vec{P} \rangle \\
&= -\mathbf{J}_{\vec{k}, \vec{P}},
\end{aligned}$$

where T is the time reversal operator and I is the inversion operator. Thus, the helicity reversal under the polarization switching is a natural consequence of the symmetry property.

The Rashba band splittings in VBM and CBM have distinctions in several respects. The angular momenta have different contributions from the spin and orbital angular momentum. In VBM, the spin angular momentum is dominant, whereas the orbital angular momentum is larger in CBM (Fig. 4.3), which comes from the original band characters of VBM and CBM. In addition, the origin of the splittings is different. The Rashba band splitting in VBM comes from the interband coupling between the s states and p states (Eq. 4.7). In contrast, the splitting in CBM comes from the intraband coupling within the $J = 1/2$ bands as well as the s - p interband coupling (Eq. 4.8). Note that the intraband splitting term (the $\vec{\gamma}_{pp}$ term in Eq. 4.8) does not have energy scale factors other than $\vec{\gamma}_{pp}$ whereas the s - p interband term contains other energy scale factors such as the hopping parameters between the s and p states and

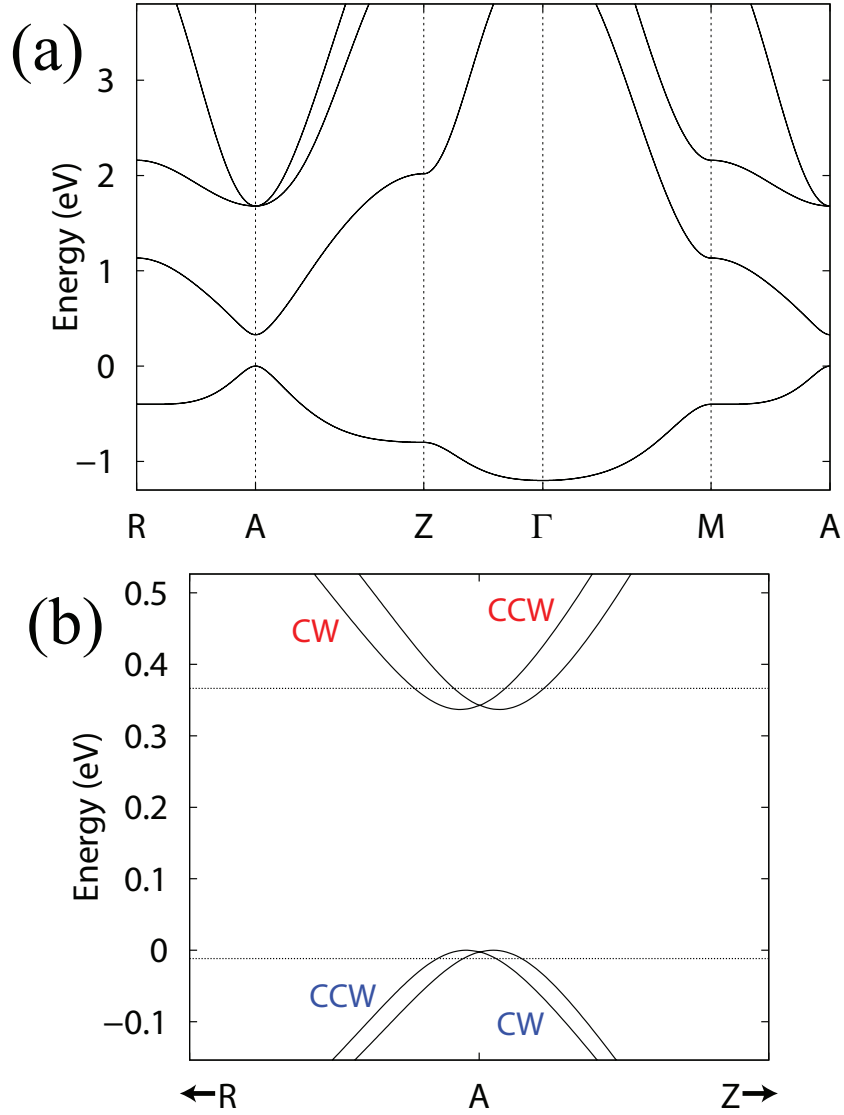


Figure 4.2: Tight-binding band structure. (a) TB band structure without the ISB field. (b) TB band structure with $\gamma_{spz}=-0.02$, $\gamma_{ppz}=-0.022$. The helical direction of the spin (orbital) angular momentum is denoted by CW or CCW in VBM (CBM) in (b). Here, CW and CCW mean clockwise and counter-clockwise, respectively.

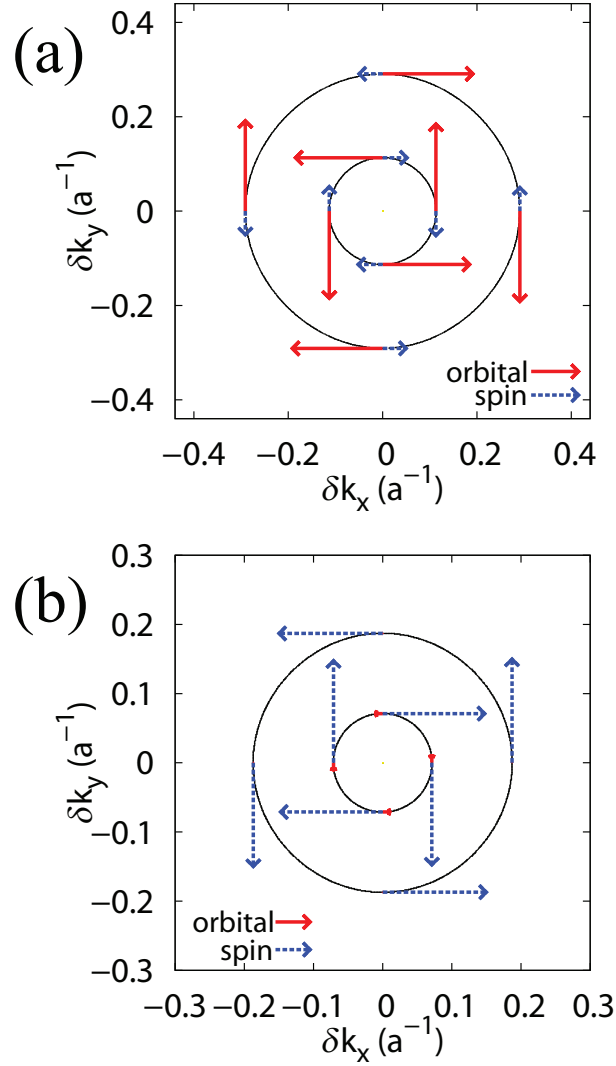


Figure 4.3: Angular momentum texture from the tight-binding calculations. (a) Angular momentum texture near the A point of BZ in CBM. (b) Angular momentum texture near the A point of BZ in VBM. The constant energy contours correspond to the energy cuts in Fig 4.2.

the SOC parameter λ .

Having the qualitative understanding from the TB model, we now turn to the realistic materials. Perovskites can have diverse structural variations and phase transitions including the ferroelectric phase [72]. To have the ferroelectric phase in perovskites, the relative sizes of the component atoms in the material are important [73]. Recently, there were experimental attempts to have a ferroelectric phase in metal halide perovskites AMX_3 by choosing organic molecules as the A component [69, 74, 75], and clear ferroelectric response is reported in those organic-inorganic hybrid materials [69]. β -MAPbI₃ is a representative example and this material shows ferroelectric property at the room temperature. Other compounds such as MASnI₃ transit to the β -phase at lower temperature and similar ferroelectric behavior is expected.

β -MAPbI₃ has a tetragonal unit cell with four formula units. There are octahedral rotations and polar distortions along the z direction in the atomic structure (Fig. 4.4(a)). The length difference between the longer and shorter Pb-I bonds resulting from the polar distortion is about 0.07 Å. Due to the enlarged unit cell ($\sqrt{2} \times \sqrt{2} \times 2$), the VBM and CBM lie at the Γ point of the BZ in the electronic band structure (Fig. 4.4(b)). There occur clear Rashba band splittings in the VBM and CBM. If we calculate the angular momentum (Fig. 4.5), the spin angular momentum dominates in VBM whereas the orbital angular momentum is larger in CBM, which is natural considering the original band characters ($S = 1/2$ VBM, $J = 1/2$ CBM). The helical directions of the two Rashba bands are opposite and will be called contrahelical (the other case will be called cohelical.). As in the previous TB analysis, the helical direction

is assigned to the spin (orbital) component in VBM (CBM). This angular momentum texture is in a good agreement with the TB result. The constant energy contours are almost isotropic. We also calculate the band dispersion changing the k_z values (Fig. 4.6). Because of the intrinsic 3D character of the material, the band structure has notable k_z dependence. (In contrast, the giant Rashba material BiTeI has a quasi-2D layered structure [76, 63].) The sizes of the Rashba splittings become smaller as we move away from the Γ point by increasing the k_z value.

The size of the Rashba splitting can be characterized by parameters such as the momentum offset \vec{k}_R , the Rashba energy E_R , and the Rashba coefficient α_R . The Rashba coefficient α_R is calculated from $\alpha_R=2E_R/k_R$. The calculated values for β -MAPbI₃ in Γ -X are $E_R = 12$ meV, $k_R = 0.015 \text{ \AA}^{-1}$, $\alpha_R = 1.5 \text{ eV\AA}$ for CBM, and $E_R = 11$ meV, $k_R = 0.016 \text{ \AA}^{-1}$, $\alpha_R = 1.4 \text{ eV\AA}$ for VBM. The calculated values for Γ -M direction are practically the same due to the isotropic character of the band structure. In the case of β -MASnI₃ for Γ -X, we find $E_R = 11$ meV, $k_R = 0.011 \text{ \AA}^{-1}$, $\alpha_R = 1.9 \text{ eV\AA}$ for CBM, and $E_R = 4$ meV, $k_R = 0.006 \text{ \AA}^{-1}$, $\alpha_R = 1.2 \text{ eV\AA}$ for VBM. The sizes of the Rashba coefficients are of order of 1 that are comparable to those of giant Rashba materials [63, 66, 67].

In our effective Hamiltonian, the angular momentum helicity in VBM was determined by $\vec{\gamma}_{sp}$ whereas that in CBM is determined by both $\vec{\gamma}_{sp}$ and $\vec{\gamma}_{pp}$. Exploiting this difference, it is possible to change the relative helicity between VBM and CBM bands by changing the values of $\vec{\gamma}_{sp}$ and $\vec{\gamma}_{pp}$ appropriately, which provides additional controllability of the relative helicity between the two

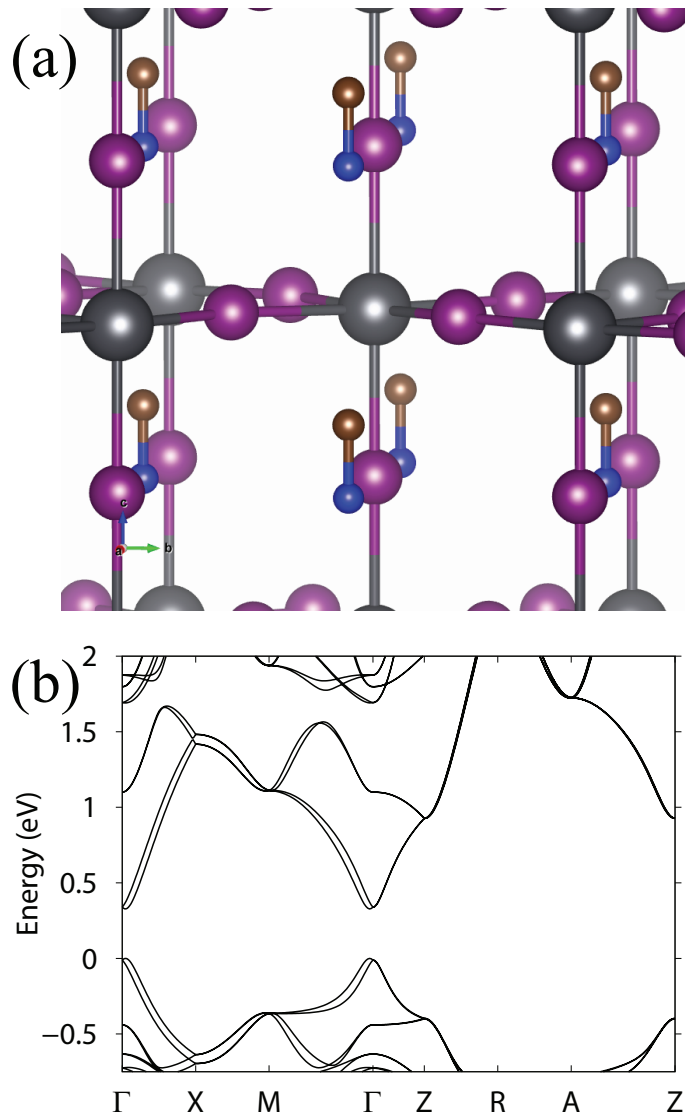


Figure 4.4: Atomic and electronic structure in the first-principles calculations. (a) Atomic structure of β -MAPbI₃. (b) Band structure of β -MAPbI₃.

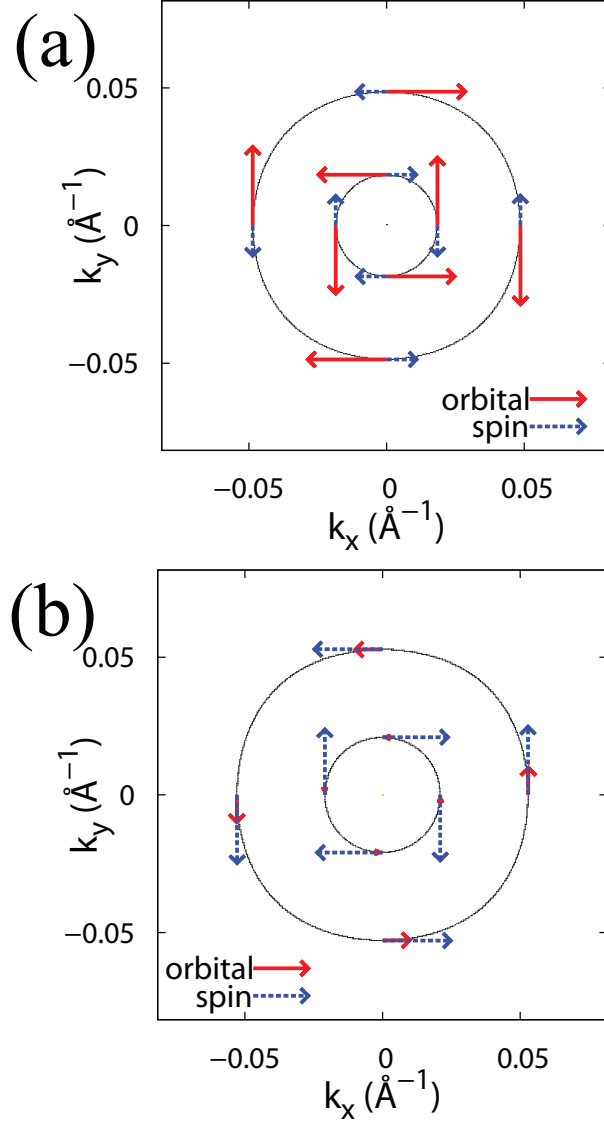


Figure 4.5: Angular momentum texture from the first-principles calculations. (a) Angular momentum texture near the Γ point of BZ in CBM. (b) Angular momentum texture near the Γ point of BZ in VBM. The constant energy contours are calculated at $\text{VBM}-\Delta E$ and $\text{CBM}+\Delta E$, where $\Delta E \approx 0.05$ eV.

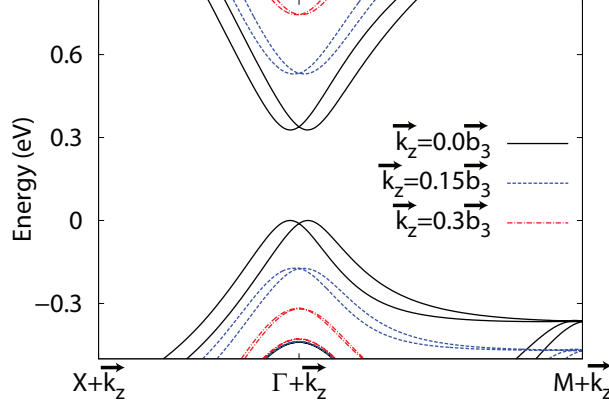


Figure 4.6: Band dispersion with different k_z . \vec{b}_3 denotes the reciprocal lattice vector along the z direction.

Rashba bands. With fixed $\vec{\gamma}_{sp}$, we compare the band structures for different $\vec{\gamma}_{pp}$. The relative helicity can be contrahelical (Fig. 4.2(b)) or cohelical (Fig. 4.7(b)). There appear band crossings within the $J = 1/2$ bands in the intermediate region (Fig. 4.7(a)). This relative helicity change can be achieved by adjusting the positions of the lateral halide atoms in real materials. We consider CsPbI₃ as the model system and set the Pb offcentering to be 2 % of the lattice constant. Then the positions of the lateral I atoms are changed along the z direction by r % of the lattice constant and we plot the band structure of the distorted system by the first-principles calculation. It is found that the helicity of the CBM bands is changed for the positive r value, and that of the VBM bands is changed for the negative r value (Fig. 4.8); the two Rashba bands are initially cohelical, but made to be contrahelical. Consequently, the positions of the lateral halide atoms are important for the relative helicity of the two Rashba bands. It should be mentioned that the helicity of the VBM Rashba

bands can be affected by other band manifolds nearby in energy (e.g., the p bands of X) if the bands couple appropriately, although in our simplified TB model only s - p coupling ($\vec{\gamma}_{sp}$) is considered for the VBM bands.

We derived the effective Hamiltonian starting from the cubic structure. Thus our model is different from 2D Rashba models that have larger effect of the crystal field asymmetry, for example, resulting in p_z -like Rashba surface bands from interband coupling [77]. In contrast, we started from the 3D cubic symmetry that has triply degenerate p bands, and the SOC induced fully spin-orbital entangled $J = 1/2$ Rashba bands. Both interband and intraband coupling occur in the $J = 1/2$ Rashba bands, and the intraband coupling term is bandgap-independent whereas the interband coupling term is bandgap-dependent.

4.1.3 Conclusions

In conclusion, we investigated the electronic structure of the ferroelectric organic-inorganic metal halide perovskites. With the experimental confirmation of the ferroelectric property, the halide perovskites were presented to be promising candidates for the ferroelectric Rashba materials, where the helical directions of the angular momentum textures in the Rashba bands can be controlled by external fields. Also, the materials have two different Rashba bands simultaneously: $S = 1/2$ Rashba bands in VBM and $J = 1/2$ Rashba bands in CBM. The controllability and characteristic band structures of the materials could be important for spintronics and optical applications.

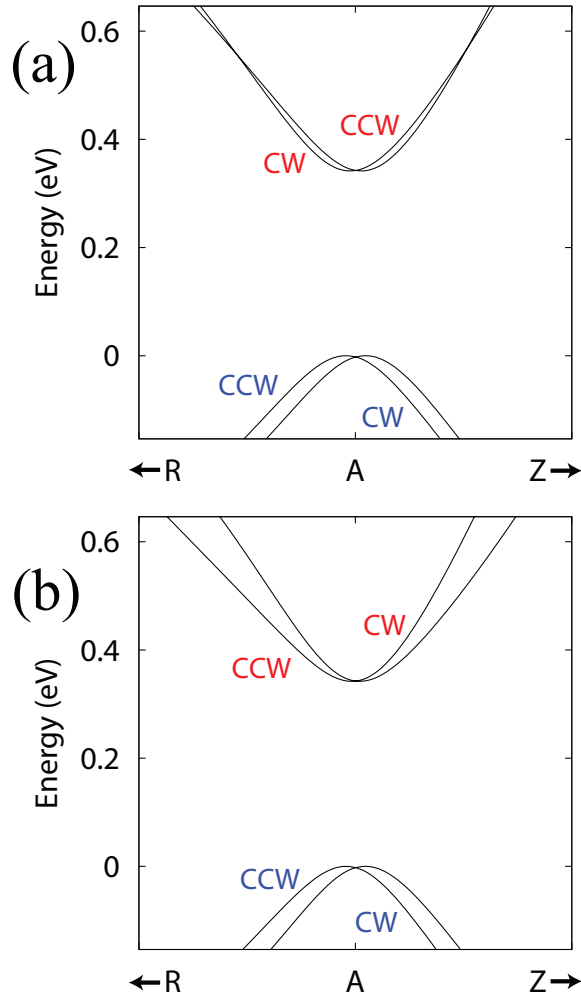


Figure 4.7: Relative helicity change between the two Rashba bands. (a) TB band structure with $\gamma_{spz}=-0.02$, $\gamma_{ppz}=0.04$. (b) TB band structure with $\gamma_{spz}=-0.02$, $\gamma_{ppz}=0.11$.

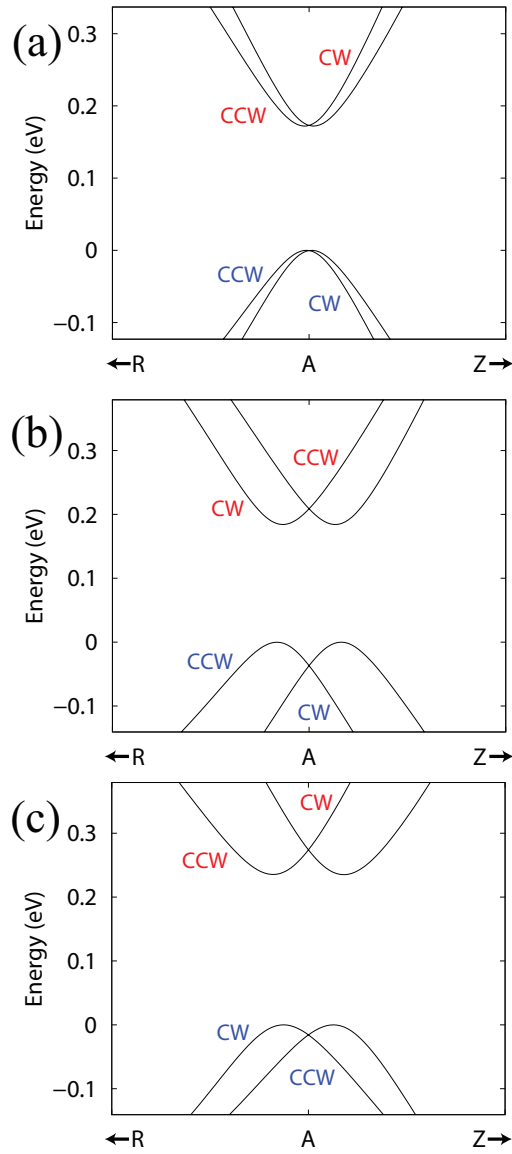


Figure 4.8: Relative helicity change in the distorted CsPbI_3 . (a) The band structure with $r = 0.0$. (b) The band structure with $r = 1.5$. (c) The band structure with $r = -1.5$.

4.1.4 Methods

We used VASP package [78, 79] to obtain the electronic structure. The PBEsol exchange-correlation functional was adopted [9]. The projector augmented-wave potentials were used [80]. A plane-wave basis set with the energy cutoff 520 eV was employed. We used the experimental atomic structure [69]. The energy contours are obtained from the interpolated band structure using Wannier functions [43, 44, 47].

Chapter 5

Summary

In this thesis, we considered two intriguing phenomena induced by the spin-orbit coupling: topological insulators and Rashba splittings. We used theoretical methods including density functional theory, Wannier functions, tight-binding approximation, and effective Hamiltonians.

In the topological insulator chapter, the realization and control of the topological phases in 2D thin films were of concern. Because of the experimental progress on the synthesis of the nano-scale materials, the theoretical consideration of nanostructures became important. In the first part, the topological quantum phase transitions by external electric fields in thin films of a 3D topological insulator Sb_2Te_3 were investigated. Considering experimental accessibility and convenience, we chose the external electric fields in the direction perpendicular to the thin films as our controlling parameter for the topological phase transition. Also, for concrete and realistic examples of our scenario, we considered thin films of one of the recently discovered tetradymite topological insulators. Using first-principles calculations based on density functional

theory, we found that the transition from a normal insulator to a topological insulator was possible in 3 QLs of Sb_2Te_3 and from a topological insulator to a normal insulator in 4 QLs. The topological invariants for the different phases were calculated directly by the lattice computation method using the wavefunctions of the *ab initio* calculation in a discretized Brillouin zone. Also, the dispersion of the boundary (edge) states was obtained from the Hamiltonian in terms of Wannier functions and confirmed to be consistent with the topological \mathbb{Z}_2 invariants. Because the external field is a practically convenient method to affect the physical system under consideration, the results would be important for the manipulation of the topological boundary states in nano-device applications. In the second part, we considered the topological phases with defect superstructures. We designed artificial defect superstructures to demonstrate that the topological narrow bands can be formed due to the topologically nontrivial spin-orbit splitting. The advantage of having topological narrow bands was that the band topology of the system could be changed by charge doping because of the narrow band width. We performed electronic structure calculations using density functional theory and showed that the Sn-Te bilayer was made to be a 2D topological insulator by introducing appropriate defect superstructures. We proposed two examples: the Sn vacancies in the 5×5 periodicity and the Te vacancies in the 5×5 periodicity with the Sb substitution and hole doping. The topological phase transitions by charge doping were possible in both cases. Using the gate voltage, charge doping in these systems could be a useful method to control the topological edge states in practice. The studies in the topological insulator part suggested

two practical mechanisms to control the band topology of the 2D thin films.

In the Rashba splitting chapter, the ferroelectric organic-inorganic metal halide perovskites were examined as candidates for the ferroelectric-coupled Rashba system. Because the Rashba splitting comes from the inversion symmetry breaking under the time-reversal symmetry and spin-orbit coupling, we considered the control of the inversion symmetry breaking polarization by employing ferroelectric materials to manipulate the spin and orbital angular momentum texture in the Rashba bands. Using the tight-binding approximation, we constructed the minimal model Hamiltonian that contained additional orbital mixings resulting from the inversion symmetry breaking field. From the tight-binding model, we derived effective Hamiltonians and qualitatively understood the splitting mechanism in the band edge states; the Rashba splitting in the valence band maximum comes from the s - p interband coupling and that in the conduction band minimum comes from the intraband coupling as well as the interband coupling. The helical angular momentum textures were reversed under the ferroelectric switching and the characteristic $S = 1/2$ and $J = 1/2$ Rashba bands with different spin and orbital composition appeared at the valence and conduction bands, respectively. Also, using the first-principles method, we calculated the electronic band structures of realistic materials such as $(\text{CH}_3\text{NH}_3)\text{PbI}_3$. We found that the material had the isotropic Rashba bands with the considerable size of the Rashba coefficient. The relative helicity changes between the $S = 1/2$ and $J = 1/2$ Rashba bands were also discussed and the positions of the lateral halide atoms could affect the relative helicity in real materials. With the experimental evidences, the ferroelectric-coupled

Rashba effect in the materials gives a realistic mechanism for the manipulation of the spin and orbital angular momentum texture in the Rashba bands and could be important in spintronic and optical applications.

Bibliography

- [1] P. Hohenberg and W. Kohn, Phys. Rev. **136** B864 (1964).
- [2] W. Kohn and L. J. Sham, Phys. Rev. **140**, A1133 (1965).
- [3] R. M. Martin, *Electronic structure: Basic theory and practical methods*, Cambridge University Press, Cambridge (2004).
- [4] J. Kohanoff, *Electronic structure calculations for solids and molecules: Theory and computational methods*, Cambridge University Press, Cambridge (2006).
- [5] D. M. Ceperley and B. J. Alder, Phys. Rev. Lett. **45**, 566 (1980).
- [6] J. P. Perdew, K. Burke, and M. Ernzerhof, Phys. Rev. Lett. **77**, 3865 (1996).
- [7] J. P. Perdew and Y. Wang, Phys. Rev. B **45**, 13244 (1992).
- [8] B. Hammer, L. B. Hansen, and J. K. Nørskov, Phys. Rev. B **59**, 7413 (1999).
- [9] J. P. Perdew, *et al.*, Phys. Rev. Lett. **100**, 136406 (2008).

- [10] U. von Barth and L. Hedin, *J. Phys. C* **5**, 1629 (1972).
- [11] P. A. M. Dirac, *Proc. R. Soc. Lond. A* **117**, 610 (1928).
- [12] P. A. M. Dirac, *Proc. R. Soc. Lond. A* **118**, 351 (1928).
- [13] J. D. Bjorken and S. D. Drell, *Relativistic Quantum Mechanics*, McGraw-Hill, Newyork (1964).
- [14] L. Kleinman, *Phys. Rev. B* **21**, 2630 (1980).
- [15] A. Mosca Conte, Ph.D. thesis (2007).
- [16] W. E. Pickett, *Comput. Phys. Rep.* **9**, 115 (1989).
- [17] G. B. Bachelet, D. R. Hamann, and M. Schlüter, *Phys. Rev. B* **26**, 4199 (1982).
- [18] L. Kleinman and D. M. Bylander, *Phys. Rev. Lett.* **48**, 1425 (1982).
- [19] G. Theurich and N. A. Hill, *Phys. Rev. B* **64**, 073106 (2001).
- [20] M. P. Surh, M.-F. Li, and S. G. Louie, *Phys. Rev. B* **43**, 4286 (1991).
- [21] L. A. Hemstreet, C. Y. Fong, and J. S. Nelson, *Phys. Rev. B* **47**, 4238 (1993).
- [22] M. S. Hybertsen and S. G. Louie, *Phys. Rev. B* **34**, 2920 (1986).
- [23] K. v. Klitzing, G. Dorda, and M. Pepper, *Phys. Rev. Lett.* **45**, 494 (1980).

- [24] D. J. Thouless, M. Kohmoto, M. P. Nightingale, and M. den Nijs, Phys. Rev. Lett. **49**, 405 (1982).
- [25] C. L. Kane and E. J. Mele, Phys. Rev. Lett. **95**, 146802 (2005).
- [26] C. L. Kane and E. J. Mele, Phys. Rev. Lett. **95**, 226801 (2005).
- [27] M. Z. Hasan and C. L. Kane, Rev. Mod. Phys. **82**, 3045 (2010).
- [28] X.-L. Qi and S.-C. Zhang, Rev. Mod. Phys. **83**, 1057 (2011).
- [29] B. Yan, C.-X. Liu, H.-J. Zhang, C.-Y. Yam, X.-L. Qi, T. Frauenheim, and S.-C. Zhang, EPL **90**, 37002 (2010).
- [30] J. Li and K. Chang, Appl. Phys. Lett. **95**, 222110 (2009).
- [31] C.-X. Liu, H. Zhang, B. Yan, X.-L. Qi, T. Frauenheim, X. Dai, Z. Fang, and S.-C. Zhang, Phys. Rev. B **81**, 041307(R) (2010).
- [32] M. Kim, C. H. Kim, H.-S. Kim, and J. Ihm, Proc. Natl. Acad. Sci. USA **109**, 671 (2012).
- [33] T. Fukui and Y. Hatsugai, J. Phys. Soc. Jpn. **76**, 053702 (2007).
- [34] T. Fukui and Y. Hatsugai, J. Phys. Soc. Jpn. **74**, 1674 (2005).
- [35] M. P. L. Sancho, J. M. L. Sancho, and J. Rubio, J. Phys. F: Met. Phys. **15**, 851 (1985).
- [36] M. P. L. Sancho, J. M. L. Sancho, and J. Rubio, J. Phys. F: Met. Phys. **14**, 1205 (1984).

- [37] H. Zhang, C.-X. Liu, X.-L. Qi, X. Dai, Z. Fang, and S.-C. Zhang, Nat. Phys. **5**, 438 (2009).
- [38] L. Fu, C. L. Kane, Phys. Rev. B **76**, 045302 (2007).
- [39] L. Fu, C. L. Kane, Phys. Rev. B **74**, 195312 (2006).
- [40] D. Xiao *et al.*, Phys. Rev. Lett. **105**, 096404 (2010).
- [41] S. Murakami, S. Iso, Y. Avishai, M. Onoda, and N. Nagaosa, Phys. Rev. B **76**, 205304 (2007).
- [42] S. Murakami and S.-i. Kuga, Phys. Rev. B **78**, 165313 (2008).
- [43] N. Marzari and D. Vanderbilt, Phys. Rev. B **56**, 12847 (1997).
- [44] I. Souza, N. Marzari, and D. Vanderbilt, Phys. Rev. B **65**, 035109 (2001).
- [45] P. Giannozzi *et al.*, J. Phys.: Condens. Matter **21**, 395502 (2009).
- [46] T. Thonhauser, T. J. Scheidemantel, J. O. Sofo, J. V. Badding, and G. D. Mahan, Phys. Rev. B **68**, 085201 (2003).
- [47] A. A. Mostofi, J. R. Yates, Y.-S. Lee, I. Souza, D. Vanderbilt, and N. Marzari, Comput. Phys. Commun. **178**, 685 (2008).
- [48] M. Bieri, *et al.*, Chem. Commun. **45**, 6919 (2009).
- [49] Z. Wang, *et al.*, Phys. Rev. B **83**, 140505(R) (2011).

- [50] F. Ye, *et al.*, Phys. Rev. Lett. **107**, 137003 (2011).
- [51] T. H. Hsieh, H. Lin, J. Liu, W. Duan, A. Bansil, and L. Fu, Nat. Commun. **3**, 982 (2012).
- [52] Y. Tanaka, Z. Ren, T. Sato, K. Nakayama, S. Souma, T. Takahashi, K. Segawa, and Y. Ando, Nat. Phys. **8**, 800 (2012).
- [53] X.-Y. Feng, H. Chen, C. Cao, and J. Dai, arXiv:1103.2538v2.
- [54] M. Kim and J. Ihm, J. Phys.: Condens. Matter **26**, 235504 (2014).
- [55] J. O. Dimmock, I. Melngailis, and A. J. Strauss, Phys. Rev. Lett. **16**, 1193 (1966).
- [56] P. B. Littlewood, *et al.*, Phys. Rev. Lett. **105**, 086404 (2010).
- [57] I. Lefebvre, M. A. Szymanski, J. Olivier-Fourcade, and J. C. Jumas, Phys. Rev. B **58**, 1896 (1998).
- [58] Y. A. Bychkov and E. I. Rashba, JETP Lett. **39**, 78 (1984).
- [59] S. LaShell, B. A. McDougall, and E. Jensen, Phys. Rev. Lett. **77**, 3419 (1996).
- [60] C. R. Ast, *et al.*, Phys. Rev. Lett. **98**, 186807 (2007).
- [61] J. H. Dil, *et al.*, Phys. Rev. Lett. **101**, 266802 (2008).
- [62] S. Mathias, *et al.*, Phys. Rev. Lett. **104**, 066802 (2010).

- [63] K. Ishizaka, *et al.*, Nat. Mater. **10**, 521 (2011).
- [64] J. Nitta, T. Akazaki, H. Takayanagi, and T. Enoki, Phys. Rev. Lett. **78**, 1335 (1997).
- [65] M. Studer, G. Salis, K. Ensslin, D. C. Driscoll, and A. C. Gossard, Phys. Rev. Lett. **103**, 027201 (2009).
- [66] D. Di Sante, P. Barone, R. Bertacco, and S. Picozzi, Adv. Mater. **25**, 509 (2013).
- [67] D. Di Sante, P. Barone, R. Bertacco, and S. Picozzi, Adv. Mater. **25**, 3625 (2013).
- [68] S. Picozzi, arXiv:1312.0095.
- [69] C. C. Stoumpos, C. D. Malliakas, and M. G. Kanatzidis, Inorg. Chem. **52**, 9019 (2013).
- [70] M. Kim, J. Im, A. J. Freeman, J. Ihm, and H. Jin, Proc. Natl. Acad. Sci. USA **111**, 6900 (2014).
- [71] H. Jin, J. Im, and A. J. Freeman, Phys. Rev. B **86**, 121102 (2012).
- [72] R. E. Cohen, Nature **358**, 136 (1992).
- [73] D. J. Singh, M. Ghita, M. Fornari, and S. V. Halilov, Ferroelectrics **338**, 73 (2006).
- [74] I. Swainson, *et al.*, Acta Crystallogr. B **66(Pt 4)**, 422 (2010).

- [75] T. Hang, W. Zhang, H. Y. Ye, and R. G. Xiong, *Chem. Soc. Rev.* **40**, 3577 (2011).
- [76] J. S. Lee, *et al.*, *Phys. Rev. Lett.* **107**, 117401 (2011).
- [77] L. Petersen and P. Hedegård, *Surf. Sci.* **459**, 49 (2000).
- [78] G. Kresse and J. Hafner, *Phys. Rev. B* **47**, 558 (1993).
- [79] G. Kresse and J. Furthmüller, *Phys. Rev. B* **54**, 11169 (1996).
- [80] P. E. Blöchl, *Phys. Rev. B* **50**, 17953 (1994).

국문 초록

스핀-궤도 결합은 전자가 원자핵 주변으로 운동하면서 생기는 유효 자기장에 전자의 스핀 자기 모멘트가 결합하면서 생기는 상대론적 현상이다. 전자 띠 구조에서 스핀-궤도 결합으로 나오는 두가지 흥미로운 현상이 있는데, 바로 위상 절연체와 라쉬바 분리이다.

위상 절연체는 전자띠의 위상으로 일반 절연체와 구분되는 새로운 양자 상이며, 위상적 경계 상태를 가지는 특징이 있다. 위상 절연체 부분에서는 2차원 박막의 전자띠 위상을 다룬다. 우선, Sb_2Te_3 박막에서 외부 전기장에 의한 위상적 양자 상전이를 고려한다. 이 물질이 박막의 두께에 따라 위상 절연체이거나 일반 절연체가 될 수 있음을 보이고 외부 전기장을 걸어서 전자띠 위상을 바꿀 수 있음을 보인다. 위상 절연체에서 일반 절연체로 전이되는 경우와 반대로 일반 절연체에서 위상 절연체로 전이되는 경우의 예를 제시한다. 두번째로, 2차원 SnTe 박막에 결합 초구조를 도입하여 위상 절연체로 만드는 방법에 대해 살펴본다. 결합 구조의 대칭성과 밀도가 적당하면 결합으로 유도된 좁은 전자띠가 안뺀한 위상을 가질 수 있음을 보인다. 결합 구조로 생기는 전자띠는 띠폭이 좁기 때문에 전하 도핑으로 그 물질의 위상을 제어할 수 있다. 전자띠 위상은 \mathbb{Z}_2 불변량을 직접 계산하는 방법과 모서리 상태의 형태를 확인하는 방법을 사용하여 알아낸다. 언급된 두가지 이

론적 제의는 위상적 상을 구현하고 제어하는데 유용할 수 있다.

라쉬바 효과는 반전 대칭 깨짐과 스핀-궤도 결합 때문에 생기는 전자띠 구조에서의 스핀 분리 현상이다. 라쉬바 분리 부분에서는 강유전 스위칭에 의한 라쉬바 분리의 방향 제어를 다룬다. 구체적으로, perovskite 구조를 가진 강유전성 유기-무기 혼합 할로겐화물의 전자띠 구조를 분석한다. 이 물질들에서 강유전성 편극이 라쉬바 띠 분리와 결합하며, 따라서 라쉬바 띠에서 각운동량 구조의 방향이 강유전성 스위칭에 의해 뒤집힐 수 있다는 것을 보인다. 또한 이 물질들은 대조되는 스핀과 오비탈 모멘트를 가진 $S = 1/2$ 와 $J = 1/2$ 라쉬바 띠가 동시에 나타나는 특징이 있다. 이런 강자성과 결합된 라쉬바 물질은 외부 전기장에 의해 스핀 자유도를 제어하는 편리한 방법을 제공할 수 있다.

주요어: 스핀-궤도 결합, 위상 절연체, 라쉬바 분리, 밀집 결합 근사, 밀도 범함수 이론

학번: 2007-20407